IMMUNOLOGY

A deubiquitination module essential for T_{reg} fitness in the tumor microenvironment

Elena Montauti[1], Samuel E. Weinberg[1], Peng Chu[2], Shuvam Chaudhuri[1], Nikita L. Mani[1], Radhika Iyer[1], Yuanzhang Zhou[2], Yusi Zhang[3], Changhong Liu[4], Chen Xin[5], Shana Gregory[1], Juncheng Wei[1], Yana Zhang[1], Wantao Chen[6], Zhaolin Sun[2]*, Ming Yan[1,6]*, Deyu Fang[1]*

The tumor microenvironment (TME) enhances regulatory T (T_{reg}) cell stability and immunosuppressive functions through up-regulation of lineage transcription factor Foxp3, a phenomenon known as T_{reg} fitness or adaptation. Here, we characterize previously unknown TME-specific cellular and molecular mechanisms underlying T_{reg} fitness. We demonstrate that TME-specific stressors including transforming growth factor–β (TGF-β), hypoxia, and nutrient deprivation selectively induce two Foxp3-specific deubiquitinases, ubiquitin-specific peptidase 22 (*Usp22*) and *Usp21*, by regulating TGF-β, HIF, and mTOR signaling, respectively, to maintain T_{reg} fitness. Simultaneous deletion of both USPs in T_{reg} cells largely diminishes TME-induced Foxp3 up-regulation, alters T_{reg} metabolic signatures, impairs T_{reg}-suppressive function, and alleviates T_{reg} suppression on cytotoxic $CD8^+$ T cells. Furthermore, we developed the first *Usp22*-specific small-molecule inhibitor, which dramatically reduced intratumoral T_{reg} Foxp3 expression and consequently enhanced antitumor immunity. Our findings unveil previously unappreciated mechanisms underlying T_{reg} fitness and identify *Usp22* as an antitumor therapeutic target that inhibits T_{reg} adaptability in the TME.

INTRODUCTION

Tumors have long been recognized as having distinctive properties of growth, invasion, and metastasis, but their ability to evade immune recognition and destruction has recently attracted attention. While neoplastic cells have sufficient antigenicity to promote an antitumor immune response, tumors evade the immune system through a variety of mechanisms including the production of immunosuppressive mediators and cytokines, defective antigen presentation, and recruitment of immunoregulatory cells such as T regulatory (T_{reg}) cells (*1*, *2*). Furthermore, the disorganized vascular system and enhanced rate of proliferation observed in tumors create a hostile microenvironment depleted of oxygen, glucose, and amino acids while enriched with cytokines, metabolic toxins, and lactic acid (*3*). Many, if not all, of these alterations in the tumor microenvironment (TME) are known to inhibit antitumor immune responses through a variety of mechanisms. In particular, these TME-derived pressures favorably alter intratumoral T_{reg} (itT_{reg}) cells, resulting in heightened proliferative and suppressive abilities, while diminishing the antitumor effects of effector T (T_{eff}) cells (*4*–*7*). Moreover, itT_{reg} cells are known to aid in metastasis, and their increased number correlates with poor clinical outcomes (*1*, *5*).

The presence of itT_{reg} cells plays a pivotal role in inhibiting antitumor immunity and is a major hurdle for current tumor-targeting immunotherapies. To enhance the effects of immunomodulatory therapies, minimizing the heightened suppression by itT_{reg} cells could significantly increase responses and overall survival across cancer types. itT_{reg} cells display up-regulated expression of the lineage-defining T_{reg} transcription factor, forkhead box P3 (Foxp3) (*8*), which is essential for proper T_{reg} function and acts to enhance T_{reg} fitness by augmenting cell stability and suppressive capabilities (*9*). However, the molecular mechanisms underlying which and how TME factors up-regulate Foxp3 expression to potentiate itT_{reg}-suppressive function remain unknown.

Although Foxp3 is uniquely important for T_{reg} identity and function, it is an intracellular protein whose targeting would require great care as complete inhibition would likely drive significant autoimmunity (*9*). In addition, specifically targeting a transcription factor like Foxp3 remains technically challenging. So, as T_{reg} depletion through a T_{reg}-specific marker remains arduous (*10*, *11*), the specific pathways that enhance T_{reg}-suppressive capabilities within the TME are attractive candidates for new therapeutic targets to diminish itT_{reg}-suppressive function. Therefore, superior therapeutic candidates will be those that control the expression and stability of Foxp3 specifically in the TME.

Foxp3 expression and stability can be regulated from the transcriptional to the posttranslational level, with each layer independently controlling the stability and overall function of T_{reg} cells. In particular, a newly appreciated layer of Foxp3 regulation and T_{reg} functional modulation is through ubiquitination (*12*, *13*). Ubiquitination of histones on the Foxp3 promoter and conserved noncoding DNA sequence regions via E3 ubiquitin ligases results in chromatin condensation and lack of Foxp3 transcription (*14*). Furthermore, direct ubiquitination of the FOXP3 protein can result in proteasomal degradation. Ubiquitin may be removed from these sites by deubiquitinating enzymes (DUBs), functioning both to open the chromatin at the transcriptional level and to stabilize FOXP3 at the protein level (*12*). The balance between E3

[1]Department of Pathology, Northwestern University Feinberg School of Medicine, 303 E. Chicago Ave, Chicago, IL 60611, USA. [2]Department of Pharmacology, Dalian Medical University, Dalian 116044, China. [3]Department of Immunology, The Fourth Military Medical University, Xi'an 710032, China. [4]Department of Thoracic Surgery, The Second Hospital of Dalian Medical University, Dalian 116021, China. [5]Department of General Surgery, The Second Hospital of Dalian Medical University, Dalian 116021, China. [6]Department of Oral Maxillofacial Head and Neck Oncology, Shanghai Ninth People's Hospital, College of Stomatology, Shanghai Jiao Tong University School of Medicine, National Clinical Research Center for Oral Diseases, Shanghai Key Laboratory of Stomatology and Shanghai Research Institute of Stomatology, Shanghai, China.
*Corresponding author. Email: fangd@northwestern.edu

ligases and DUBs on Foxp3 expression results in an equilibrium state that regulates Foxp3 levels within T_{reg} cells. We and others have discovered three members of the ubiquitin-specific peptidase (USP) family as direct modulators of Foxp3 deubiqutination at the transcriptional and/or posttranslational level: *Usp7*, *Usp21*, and *Usp22* (*12*–*16*). However, the broad environmental cues and cellular regulation of these deubiquitinases remain unknown. Here, we investigate the role of the TME on the USP-Foxp3 axis and identify specific TME factors that selectively induce *Usp22* and *Usp21* expression to control T_{reg} stability and adaptation. Last, we develop the first *Usp22*-specific inhibitor capable of antitumor activity, demonstrating the importance of targeting T_{reg} adaptability within the TME.

RESULTS

Selective up-regulation of Foxp3 deubiquitinases *Usp22* and *Usp21* in itT_{reg} cells

To determine how the TME affects tumor immunity, we first characterized the tumor infiltrated T_{reg} cells using multiple syngeneic tumor models including B16 melanoma, LLC1 Lewis lung carcinoma, and EG7 lymphoma. Both the percentages of and FOXP3 protein levels are increased in itT_{reg} cells relative to splenic T_{reg} cells within the same mouse as well as the control non-tumor mouse (fig. S1, A to C). Furthermore, itT_{reg} cells in each tumor type exhibited increased surface expression of multiple known T_{reg}-suppressive markers including CTLA-4 and PD-1 (fig. S1, D to G). These data suggest that itT_{reg} cells have elevated immunosuppressive functions through the up-regulation of Foxp3 and surface inhibitory receptors, which is consistent with previous studies demonstrating that human itT_{reg} cells display enhanced suppressive function (*7*).

As multiple Foxp3-stabilizing USPs have been recently identified (*14*–*16*), we hypothesized that modulation of their expression may drive the Foxp3 up-regulation in itT_{reg} cells. The mRNA level of *Usp22* was consistently increased within itT_{reg} cells in comparison to the peripheral T_{reg} cells harvested from the same mouse, but the *Usp7* mRNA level was unchanged. In contrast, the *Usp21* mRNA level was only increased under B16 but not LLC1 and EG7, suggesting that *Usp21* up-regulation in T_{reg} cells occurs only under certain TME conditions (Fig. 1, A to C). None of the Usp levels were altered in intratumoral CD8 T cells compared to peripheral, splenic CD8 T cells (fig. S2A). These data indicate that one or many factors in the TME up-regulate both *Usp22* and *Usp21* transcription to stabilize Foxp3 specifically for T_{reg} fitness. We also detected an upward, but statistically yet to be significant, trend of *USP22* in T_{reg} cells from human lung tumor tissues (LTu) in comparison to adjacent healthy lung tissue (AHL) (fig. S2B). This USP22 up-regulation shows a positive association with *FOXP3* up-regulation within the LTu patient samples (fig. S2C). Consistent with our observation from the syngeneic lung cancer model, *Usp21* was not increased in human lung tumor itT_{reg} cells, nor did it have a significantly positive correlation with *Foxp3* (fig. S2, C and D), suggesting that *Usp22* is the more dominant USP in T_{reg} cells within the tumor in the context of lung cancer. Together with our recent discovery that *Usp22* functions as a Foxp3-specific deubiquitinase, our data suggest that *Usp22* promotes Foxp3 expression in itT_{reg} cells *(14)*.

Tumor-derived TGF-β selectively induces *Usp22* and *Usp21* in T_{reg} cells

To identify the TME factors involved in inducing *Usp22* and *Usp21* expression in T_{reg} cells, we began with testing whether any tumor-derived soluble factors are involved by coculturing in vitro induced T_{reg} (iT_{reg}) cells with tumor-conditioned medium (TCM). TCM from B16 and LLC1, but not EG7 cells, enhanced *Usp22* and *Usp21* mRNA levels (Fig. 2A). In contrast, the levels of *Usp7* remained unchanged, recapitulating the results in Fig. 1. Similar to the mRNA levels, USP22 and USP21 protein levels were increased upon incubation with LLC1 TCM (Fig. 2B). Consistently, the addition of EG7 cultured medium did not enhance any of the USPs at the protein level (Fig. 2B), confirming that specific tumor types selectively induce Foxp3 deubiquitinases in T_{reg} cells.

Many types of tumors secrete large amounts of transforming growth factor–β (TGF-β), which dampen immune responses and promote metastasis (*17*, *18*). Together with the fact that TGF-β is particularly important for iT_{reg} generation and stability (*19*), we speculated that TGF-β could enhance Foxp3 expression in iT_{reg} cells through induction of *Usp22* and *Usp21*. mRNA levels of both *Usp22* and *Usp21*, but not *Usp7*, were increased when TGF-β was added to the medium of iT_{reg} cells (fig. S3, A and B). This increase of both *Usp22* and *Usp21* expression was largely diminished by the addition of a TGF-β inhibitor (LY 3200882) (fig. S3C). The level of Foxp3 mRNA rose concurrently with the levels of *Usp22* and *Usp21* (fig. S3D), demonstrating that TGF-β can further enhance Foxp3 expression through *Usp22* and *Usp21* induction. To support this notion, we further demonstrated that the TGF-β inhibitor completely diminished the TCM-induced mRNA enhancement of *Usp22* (Fig. 2C), signifying that TGF-β is the primary factor in the B16 and LLC1 TCM that enhances *Usp22* expression. The *Usp21* mRNA level was diminished when the inhibitor was added to the LLC1 TCM, but not under B16 TCM condition (Fig. 2C). It is possible that this difference could be due to the quantity of TGF-β secreted by the tumor cell lines into the medium. LLC1 cells secreted significantly higher amounts of TGF-β than both B16 and EG7 cells (fig. S3E), which positively correlates with observed increase in *Usp22* and *Usp21* mRNA expression (fig. S3, F and G). The levels of *Usp7* remain unchanged under all treatment groups and displayed no correlation to the increasing level of TGF-β in the various tumor types (Fig. 2C and fig. S3, B, C, and H).

TGF-β signaling up-regulates *Usp22* and *Usp21* through distinctive pathways

To uncover the mechanism by which TGF-β acts on *Usp22* and *Usp21* transcription, we first investigated the canonical TGF-β signaling pathway, which works through the coactivating SMAD [homologs of the *Drosophila* protein, mothers against decapentaplegic (Mad), and the *Caenorhabditis elegans* protein Sma] transcription factors: SMAD2, SMAD3, and SMAD4 by specifically binding to the SMAD-binding element (SBE) (*20*, *21*). We scanned along the promoter regions of both *Usp22* and *Usp21* for sequences of conserved SBE. Along the *Usp22* promoter, we found promising regions for which we made primers and assessed the SMAD-binding capacity (fig. S4, A and B). Chromatin immunoprecipitation (ChIP) analysis detected that SMAD3 and SMAD4, but not SMAD2, bind to *Usp22* promoter at around 300 and 1200 base pairs upstream of the transcription start site (fig. S4B). SMAD

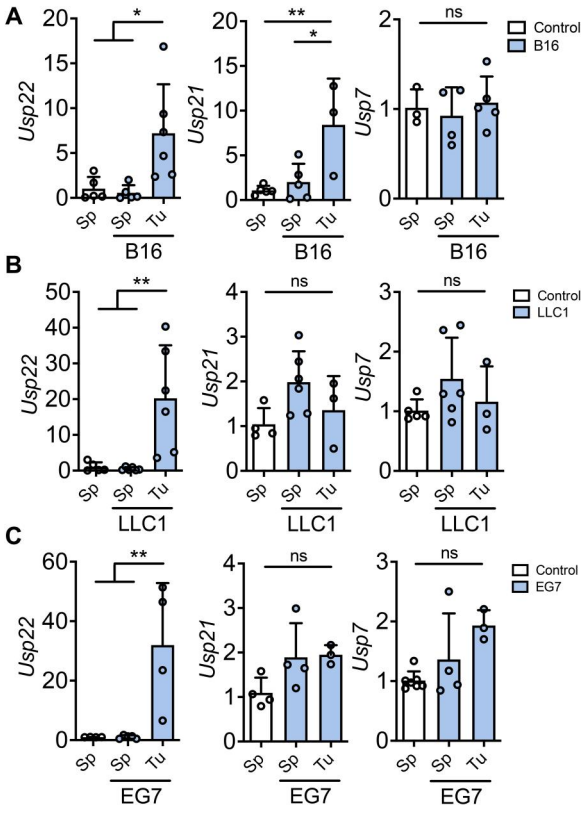

Fig. 1. Intratumoral T_{reg} cells have increased mRNA expression of *Usp22* and *Usp21*. (**A** to **C**) mRNA level of YFP^+ sorted T_{reg} cells from control mice spleens and tumor-challenged mice spleens (Sp) and tumor cells (Tu). All mRNA values were calculated relative to WT T_{reg} cell levels of unchallenged mice. Spleens: B16: *Usp22*: $n = 5$ to 6, *Usp21*: $n = 3$ to 5, and *Usp7*: $n = 3$ to 5; LLC1: *Usp22*: $n = 5$ to 6, *Usp21*: $n = 3$ to 6, and *Usp7*: $n = 3$ to 6; EG7: *Usp22*: $n = 4$ to 5, *Usp21*: $n = 3$ to 4, and *Usp7*: $n = 3$ to 7. (A to C) Two-tailed unpaired *t* test was done to determine statistical significance. All data are presented as means ± SD. ns, not significant. $^*P < 0.05$, $^{**}P < 0.01$.

binding at both sites was ablated upon the addition of the TGF-β inhibitor, demonstrating that SMAD3 and SMAD4 binding to the *Usp22* promoter is due directly to TGF-β signaling (Fig. 2D). SMAD2 showed no binding capacity to any regions of the *Usp22* promoter (Fig. 2D and fig. S3B), likely due to steric hindrance blocking its direct DNA interaction (*22*).

Although *Usp22*-null iT_{reg} cells polarize normally with high levels of TGF-β, suboptimal polarization conditions with low TGF-β resulted in a significant decrease in FOXP3 mean fluorescence intensity (MFI) and percentage relative to the wild-type (WT) iT_{reg} cells (*14*), implying that *Usp22* perpetuates TGF-β signaling for iT_{reg} polarization. *Usp22*-null iT_{reg} cells display a significant reduction in both SMAD2 and SMAD4 protein levels compared to WT iT_{reg} cells, but no difference in their mRNA levels (fig. S4, C and D), suggesting that *Usp22* functions as a positive regulator for the TGF-β signaling pathway by stabilizing SMAD proteins. *Usp22* interacts with and deubiquitinates both SMAD2 and SMAD4 (fig. S4, E, F, and H). Although *Usp22* interacts with SMAD3, it does not act as a DUB of SMAD3 (fig. S4, E and G), suggesting that it acts specifically to regulate TGF-β pathway by stabilizing SMAD2 and SMAD4. In particular, *Usp22*-null iT_{reg} cells displayed enhanced degradation of SMAD2 and SMAD4, which is rescued upon proteasomal inhibition with MG132 treatment (fig. S4, I and J). Therefore, our data suggest that *Usp22* functions to reciprocally enhance TGF-β signaling through SMAD2 and SMAD4 protein stabilization. This act ensures up-regulation of itself through a positive feedback loop, further ensuring Foxp3 expression in itT_{reg} cells. The phenomenon induced by TGF-β in iT_{reg} cells is not recapitulated in natural T_{reg} (nT_{reg}) cells, where development is independent of TGF-β (fig. S5, A and B), suggesting that the induction of Usps by TGF-β is unique but critical to iT_{reg} cells. Consistently, SMAD2 degradation was not altered in nT_{reg} cells, suggesting that the Smad feedback loop is most important in TGF-β–sensitive iT_{reg} cells (fig. S5C).

Unlike with *Usp22*, no SBEs were found when scanning the *Usp21* promoter. None of the regions showed binding capacity of any of the tested SMAD proteins as analyzed by ChIP assay, confirming that *Usp21* expression is not induced through canonical TGF-β signaling (fig. S6A). However, the lack of *Usp21* in iT_{reg} cells results in reduced Foxp3 expression in vitro, leaving the opportunity for noncanonical TGF-β signaling to drive *Usp21* induction and result in stabilization of FOXP3 (fig. S6, B to D). Inhibition of p38, a Smad-independent TGF-β–activated mitogen-activated protein kinase (MAPK), restrained TGF-β–mediated *Usp21* induction (fig. S6E). Together, these data indicate that *Usp22* and *Usp21* are mediated through distinct TGF-β signaling pathways, and the TGF-β–induced *Usp22* as positive feedback to stabilize SMAD2 and SMAD4 (fig. S6F).

Hypoxia selectively induces T_{reg} *Usp22*, which supports Foxp3 expression

In addition to tumor cell–secreted factors, tumor-driven hypoxia has been repeatedly implicated in Foxp3 stability and T_{reg} cell function (*23*, *24*). A known negative prognostic factor in solid tumors (*3*, *25*), hypoxia preferentially down-regulates T cell proliferation, receptor signal transduction, and effector function while increasing T_{reg} cell–suppressive capabilities (*23*, *26*, *27*). We, therefore, investigated the effects of hypoxia on Foxp3-stabilizing USP levels in T_{reg} cells. Unexpectedly, only *Usp22* expression was enhanced under hypoxic conditions at both the mRNA and protein levels (Fig. 3A and fig. S7A). Therefore, we speculated that *Usp22* could function as a stabilizer of Foxp3 under the hypoxic conditions in the TME and performed a Foxp3 stability assay. *Usp22*-deficient T_{reg} cells show a reduced ability to sustain Foxp3 expression under hypoxic conditions (Fig. 3B and fig. S7B), signifying that *Usp22* is required for Foxp3 stabilization under the hypoxic conditions found within the TME.

In hypoxic conditions, hypoxia-inducible factor–α (HIF-α) is stabilized, resulting in the activation of a transcriptional program that promotes cellular adaptation to low oxygen levels (*28*). HIF-α is known to have two functional binding sites on the *Usp22* promoter (*29*), suggesting that hypoxic induction of *Usp22* may be HIF-α dependent. Incubation with hypoxia-independent HIF-α activator, dimethyloxalylglycine (dMOG), increased *Usp22* mRNA levels in T_{reg} cells (Fig. 3C), indicating that HIF-α–induced *Usp22* expression is involved in Foxp3 stabilization. To support this, we further showed that *Usp22*-deficient T_{reg} cells displayed decreased stability of Foxp3 following treatment with dMOG, confirming that *Usp22*-dependent Foxp3 stabilization under hypoxic conditions is HIF-α dependent (fig. S7, C and D). These results demonstrate the

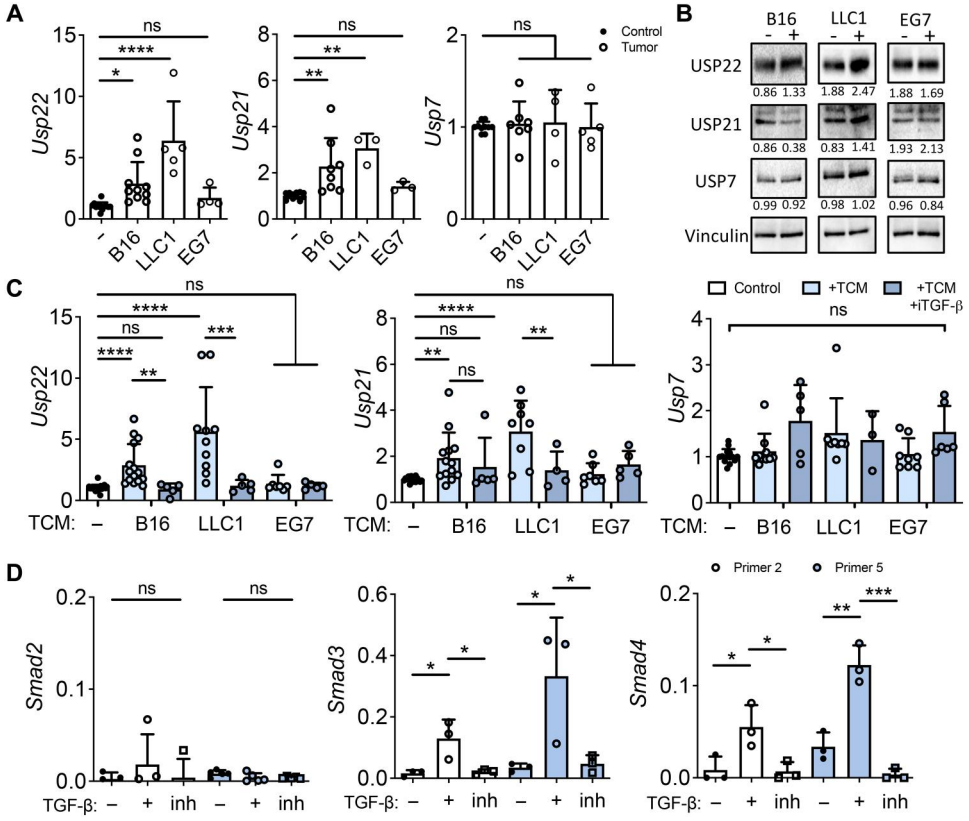

Fig. 2. Tumor cell–secreted TGF-β increases *Usp22* and *Usp21* level in iT_{reg} cells. (**A**) USP mRNA level in iT_{reg} cells in control T cell medium compared to addition of tumor cell–treated medium at 50:50 with T cell medium for 24 hours. *Usp22*: control: $n = 14$, B16: $n = 10$, LLC1: $n = 5$, and EG7: $n = 4$. *Usp21*: control: $n = 12$, B16: $n = 8$, LLC1: $n = 3$, and EG7: $n = 3$. *Usp7*: control: $n = 10$, B16: $n = 7$, LLC1: $n = 4$, and EG7: $n = 5$. (**B**) USP protein level in iT_{reg} cells in control T cell medium compared to addition of tumor cell–treated medium at 50:50 with T cell medium for 24 hours. The relative protein expression levels were quantified using Bio-Rad Image software and normalized with the loading controls. (**C**) USP mRNA level in iT_{reg} cells with the addition of a TGF-β inhibitor in tumor cell medium. *Usp22*: control: $n = 22$, B16: $n = 15$, B16 + inhibitor (inh): $n = 5$, LLC1: $n = 10$, LLC1 + inh: $n = 5$, EG7: $n = 7$, and EG7 + inh: $n = 5$. *Usp21*: control: $n = 20$, B16: $n = 13$, B16 + inh: $n = 5$, LLC1: $n = 8$, LLC1 + inh: $n = 4$, EG7: $n = 7$, and EG7 + inh: $n = 5$. *Usp*7: control: $n = 14$, B16: $n = 10$, B16 + inh: $n = 5$, LLC1: $n = 8$, LLC1 + inh: $n = 3$, EG7: $n = 8$, and EG7 + inh: $n = 6$. (**D**) SMAD2, SMAD3, and SMAD4 binding capacity along the *Usp*22 promoter under TGF-β inhibition. SMAD2: $n = 4$ to 5, SMAD3: $n = 3$, and SMAD4: $n = 3$. (A to C) All mRNA values were calculated relative to untreated WT iT_{reg} cells. (A to D) Ordinary one-way ANOVA with multiple comparisons was performed to determine significance. All data are presented as means ± SD. *$P < 0.05$, **$P < 0.01$, ***$P < 0.001$, and ****$P < 0.0001$.

importance of *Usp22* in hypoxia-regulated Foxp3 expression within the TME.

Metabolic alterations in the TME induce *Usp22* and *Usp21* to promote Foxp3 stability

In addition to oxygen, glucose levels in the TME are often decreased, in part, through its enhanced uptake by tumor cells, which compete with the glucose necessity of the highly glycolytic T_{eff} cells (*30*, *31*). Conversely, Foxp3 promotes oxidative phosphorylation over glycolysis in T_{reg} cells, potentially giving them a functional advantage within the TME (*4*, *32*, *33*). Therefore, we hypothesized that the observed T_{reg} cell advantage in nutrient-deprived environments could exist partially by inducing Foxp3-stabilizing USP expression. The mRNA and protein levels of *Usp22*, but not *Usp21* and *Usp7*, were increased in T_{reg} cells upon glucose deprivation (Fig. 3D and fig. S4E). In addition, *Usp22*-deficient T_{reg} cells have significantly lower Foxp3 stability under glucose deprivation compared to WT T_{reg} cells, demonstrating that *Usp22* maintains Foxp3 levels under glucose-restricted conditions (Fig. 3E and fig. S7F).

In addition, a scarcity of amino acids within tumors also alters immune cell function (*31*), and amino acid starvation is known to enhance T_{reg} cell induction (*34*). To investigate the role of USPs in amino acid starvation–induced Foxp3 expression, we cultured T_{reg} cells in medium lacking amino acids. Amino acid starvation led to increased expression of both *Usp22* and *Usp21*, but not *Usp7*, in T_{reg} cells (Fig. 3F). Furthermore, the stability of Foxp3 in amino acid–starved T_{reg} cells is reduced by the deficiency of *Usp22* or *Usp21* (Fig. 3G and fig. S7G).

In environments depleted of both glucose and amino acids, activation of adenosine monophosphate–activated protein kinase (AMPK) suppresses anabolic metabolism while up-regulating oxidative metabolism to promote cellular survival (*35*), prompting us to uncover whether AMPK activation is involved in *Usp22* or *Usp21* up-regulation. We therefore treated T_{reg} cells with two AMPK activators: an inhibitor of mitochondrial adenosine triphosphate (ATP) synthase, oligomycin A, and a direct AMPK activator, AICAR. While oligomycin A treatment increased both *Usp22* and *Usp21*, but not *Usp7*, in T_{reg} cells, AICAR treatment was unable to up-regulate any Usps (Fig. 3H and fig. S7H). Oligomycin A functions to

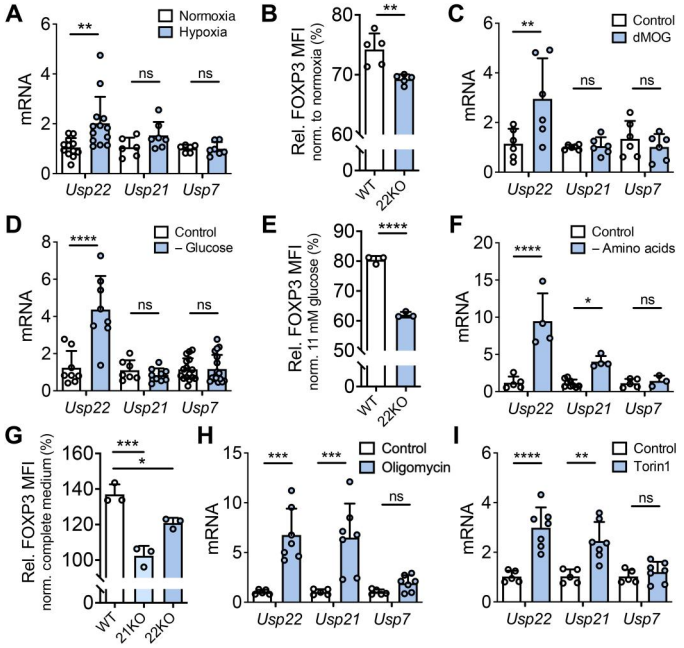

Fig. 3. *Usp*22 and *Usp*21 are required for Foxp3 stability in T_{reg} cells under environmental and metabolic stress found in the TME. (**A**) T_{reg} USP mRNA level under normoxic (21% O_2) versus hypoxic (1% O_2) conditions after 24 hours ($n = 6$ to 13). (**B**) Foxp3 MFI change in 22KO T_{reg} cells relative to WT T_{reg} cells after 72 hours under normoxic (21% O_2) versus hypoxic (1% O_2) conditions. Assessed by calculating Foxp3 change under hypoxic conditions relative to WT and 22KO respective controls ($n = 5$). (**C**) T_{reg} USP mRNA level after treatment with dMOG for 24 hours ($n = 6$). (**D**) USP mRNA level in T_{reg} cells after exposure to glucose-restricted (0.5 mM) conditions after 24 hours relative to normal medium (11 mM glucose) ($n = 7$ to 18). (**E**) Relative Foxp3 MFI change in T_{reg} cells from control and cells cultured under low-glucose conditions after 48 hours. Assessed by calculating Foxp3 change under low-glucose conditions relative to WT and 22KO T_{reg} cell Foxp3 MFI respective controls ($n = 3$). (**F**) T_{reg} USP mRNA level under amino acid starvation for 24 hours ($n = 5$ to 9). (**G**) Foxp3 MFI stability in *Usp*22- or *Usp*21-null T_{reg} cells cultured under normal medium conditions versus amino acid starvation after 48 hours ($n = 3$). Assessed by calculating Foxp3 change under amino acid starvation conditions relative to WT and 22KO respective controls. (**H**) T_{reg} USP mRNA level after treatment with 1 μM oligomycin A for 24 hours ($n = 5$ to 7). (**I**) T_{reg} USP mRNA level after treatment with 250 nM Torin1 for 24 hours ($n = 5$ to 7). (A, C, D, F, H, and I) Ordinary one-way ANOVA with multiple comparisons was performed to determine significance. (B, E, and G) Two-tailed unpaired *t* test was performed to determine statistical significance. All data are presented as means ± SD. $^*P < 0.05$, $^{**}P < 0.01$, $^{***}P < 0.001$, and $^{****}P < 0.0001$. All mRNA values calculated relative to unchallenged WT T_{reg} cells.

acutely activate AMPK by increasing the adenosine monophosphate (AMP) to ATP ratio, but it is also known to activate other cellular stress response pathways independent of AMPK activity. Specifically, oligomycin A induces chronic mammalian target of rapamycin (mTOR) inhibition through an ATF4-dependent pathway, which is independent of AMPK (*36*). Therefore, environmental sensing of glucose and amino acid shortages may up-regulate Usps through the mTOR pathway. Direct mTOR inhibition through Torin1 increases *Usp22* and *Usp21* mRNA expression in T_{reg} cells (Fig. 3I). Both oligomycin A treatment and mTOR inhibition are shown to enhance Foxp3 expression in T_{reg} cells, suggesting that mTOR activity modulates Foxp3 expression and stability through *Usp22*, and to a lesser extent *Usp21*, in T_{reg} cells (fig. S7I) (*35*, *37*–*39*).

Usp22 and *Usp21* modulate T_{reg} fitness through distinct pathways

Our discoveries thus far have suggested that *Usp22* and, to a lesser extent, *Usp21* are important in maintaining Foxp3 expression in the TME through multiple pathways. To study their combined functionality in vivo, we generated a strain of T_{reg}-specific *Usp22* and *Usp21* double knockout (dKO) mice by breeding *Usp21*$^{f/f}$ mice with *Usp22*$^{f/f}$Foxp3^{YFPcre} single KO mice. This breeding strategy gave us the T_{reg}-specific KO of *Usp22* (22KO), *Usp21* (21KO), and the dKO, all of which were confirmed via quantitative polymerase chain reaction (qPCR) (Fig. 4A). Deletion of either *Usp22*, *Usp21*, or both in T_{reg} cells did not alter the frequency of either B or T cells in the spleens of 6-week-old mice (fig. S8, A and B). While the mice display similar weights early in life, by 24 weeks of age, the 22KO and dKO animals are consistently smaller in size compared to WT (Fig. 4B).

Unsurprisingly, all three KO groups showed a significant increase in CD44^{hi}CD62^{Lo}-activated splenic T_{eff} cells in comparison to age-matched WT mice, consistent with the development of low-level, progressive inflammation with age (Fig. 4C). Of note, only the 22KO and dKO mice showed decreases in Foxp3 expression and significant reductions in T_{reg} cell–associated suppressive markers (Fig. 4, D and E). Consistently, a previous study reported that the 21KO mice develop age-related impairments in T_{reg} cell function and number secondary to impaired Foxp3 expression, whereas 8-week-old young mice showed no changes in Foxp3 expression (*16*). Transcriptional profiling revealed that more T_{reg} cell–suppressive markers were differentially expressed in the dKO mice than in either single KO mice when compared to WT gene expression (Fig. 4E), suggesting synergism between the loss of *Usp22* and *Usp21* on T_{reg} cell stability and function. Furthermore, differentially expressed genes (DEGs) between the 21KO and 22KO mice were relatively distinct (Fig. 4F). Although gene set enrichment analysis (GSEA) of both single KO mice showed changes in several cell cycle and proliferative pathways, such as G_2-M checkpoints and E2F targets, as well as changes in oxidative phosphorylation (Fig. 4G), there were only a total of 32 overlapping DEGs between the 21KO and 22KO mice (Fig. 4F). T_{reg} cells from the dKO mice displayed a GSEA and bulk gene expression signature that merged the changes found in each of the single KO mice, suggesting that the loss of both *Usp22* and *Usp21* synergizes to diminish T_{reg} cell function (Fig. 4G) in both Foxp3-depedent and Foxp3-independent manner.

As we demonstrated that both *Usp22* and *Usp21* are regulated by metabolic alterations in the TME, it was particularly interesting to identify disruption of multiple metabolic pathways in each of the KO groups. T_{reg} cells from dKO mice had profound changes in lipid metabolic processes, one-carbon metabolism, and ribosomal biogenesis (fig. S8, C to E). When compared to the DEGs in the dKO T_{reg} cells, *Usp22*-null T_{reg} cells, but not *Usp21*-deficient cells, displayed similar alterations in both lipid metabolism and one-carbon metabolism to the dKO T_{reg} cells (fig. S8, C and D). In contrast, T_{reg} cells from the 21KO and dKO mice showed profound decreases in ribosomal gene expression, which was not identified in the *Usp22*-null T_{reg} cells (fig. S8E), suggesting distinct pathways by which *Usp22* and *Usp21* modulate T_{reg} fitness. Our in vitro metabolic flux analyses further demonstrate that, unlike the 21KO mice,

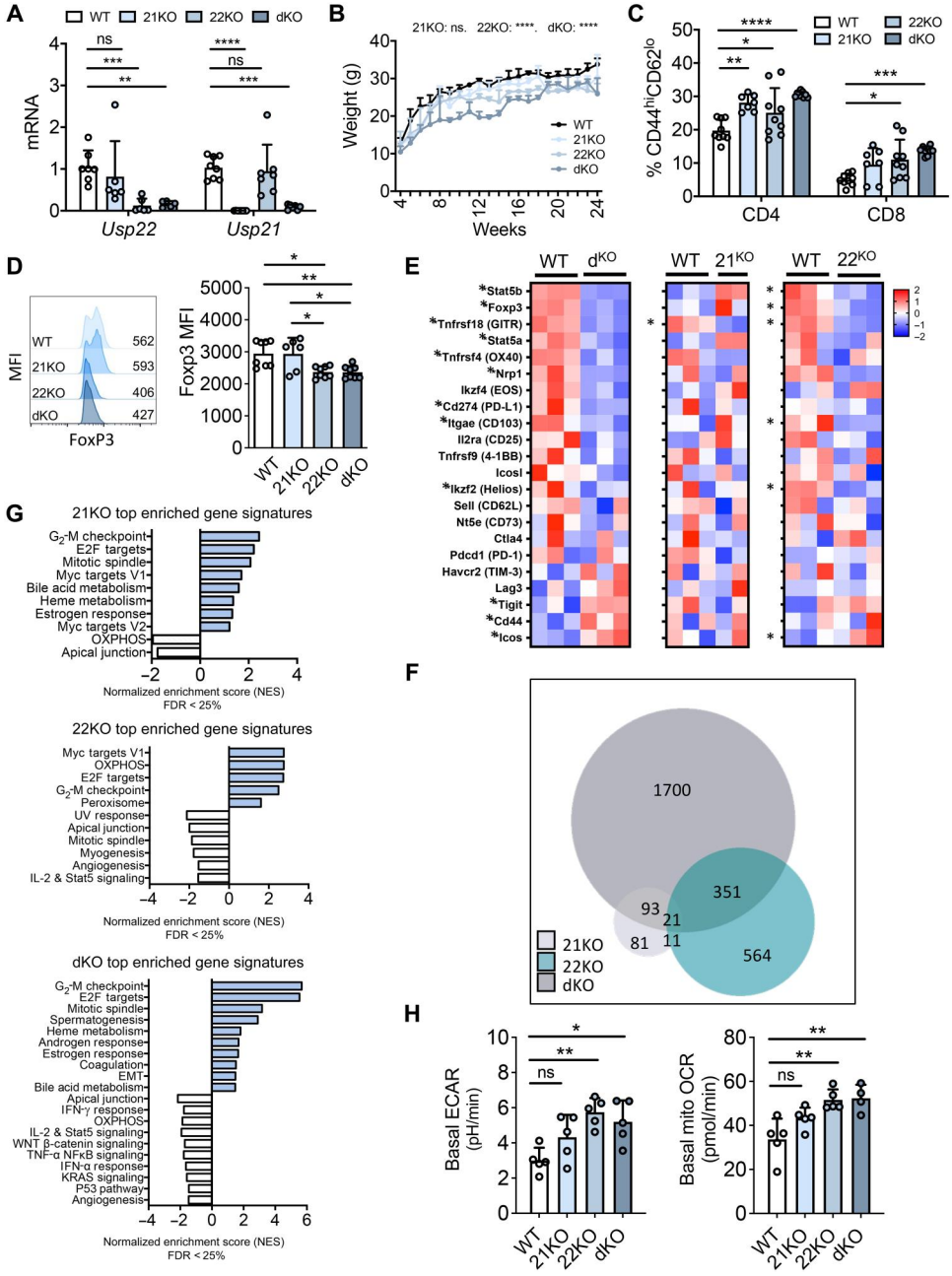

Fig. 4. Loss of *Usp*22 and *Usp*21 in T_{reg} cells differentially impairs Foxp3 expression and cell function. (**A**) *Usp*22 and *Usp*21 levels in WT, 21KO, 22KO, and dKO mice ($n = 5$ to 8). All mRNA values were calculated relative to WT T_{reg} cells. (**B**) Mice weights over a 2-month period ($n = 2$ to 9). (**C**) Peripheral activation of $CD4^+$ and $CD8^+$ T cells as measured by $CD44^{hi}CD62L^{lo}$ expression ($n = 7$ to 9). (**D**) Representative histogram (left) and quantification (right) of Foxp3 MFI in splenic T_{reg} cells of WT and KO animals ($n = 6$ to 8). (**E**) Heatmap of T_{reg} cell signature genes (*significance is adjusted $P < 0.01$) in 21KO ($n = 2$), 22KO ($n = 3$), and dKO ($n = 3$) versus WT ($n = 3$) mice. Genes ordered by decreased to increased differential expression in dKO mice. (**F**) Venn diagram of DEGs (adjusted $P < 0.01$) between 22KO, 21KO, and dKO ($n = 2$ to 3). (**G**) Normalized enrichment scores from GSEA (FDR < 25%) from the hallmark gene set in the Molecular Signatures Database comparing the gene set generated from RNA sequencing of WT, 21KO, 22KO, and dKO mice ($n = 2$ to 3). (**H**) Basal mitochondrial OCR and basal ECAR of 21KO ($n = 5$), 22KO ($n = 5$), and dKO ($n = 4$ to 5) relative to WT ($n = 5$) T_{reg} cells. (A to C) Two-way ANOVA with multiple comparisons between rows was performed to determine statistical significance. (D and H) One-way ANOVA with multiple comparisons between rows was performed to determine statistical significance. All data are presented as means ± SD. *$P < 0.05$, **$P < 0.01$, ***$P < 0.001$, and ****$P < 0.0001$.

both the 22KO and dKO mice display enhanced mitochondrial oxygen consumption rate (OCR) and extracellular acidification rate (ECAR) (Fig. 4H), suggesting that *Usp22* may play a dominant and essential role in modulating the metabolic state of T_{reg} cells.

As *Usp21* seemed to have a Foxp3-independent role in T_{reg} function, we compared the DEGs from the 22KO and dKO mice to determine the contribution of *Usp21* to the dKO phenotype. We noticed significant changes in cell cycle pathways and effector differentiation pathways (fig. S8F), suggesting a loss of homeostasis in the T_{reg} compartment. An increase in proliferation of the 21KO and dKO T_{reg} cells in comparison to WT T_{reg} cells, but not in the 22KO T_{reg} cells (fig. S8G), suggests that the normally highly suppressive effector T_{reg} population has an increased proliferative capacity with a down-regulation of functional genes, generally suggestive of a dysfunctional suppressive capacity (*40*). Collectively, these data imply that both *Usp22* and *Usp21* modulate T_{reg} cell metabolism, although seemingly through unique pathways to maintain T_{reg} stability and function.

Usp22 and *Usp21* deletion in T_{reg} cells synergizes to enhance antitumor immunity

To test the importance of T_{reg} cell *Usp22* and *Usp21* in tumor conditions in vivo, we used the B16 melanoma syngeneic tumor model. Mice with T_{reg}-specific ablation of *Usp22* showed increased tumor rejection compared to the deletion of *Usp21*. Importantly, though, mice harboring the joint deletion of both *Usp22* and *Usp21* in T_{reg} cells grew the smallest tumors (Fig. 5A). In addition, the dKO and 22KO animals showed greater proportions of effector memory $CD8^+$ T cells in the spleens (Fig. 5B). In contrast, deletion of *Usp21* in T_{reg} cells was insufficient to enhance the B16 tumor rejection (Fig. 5A). Consistently, 21KO mice effector memory populations and cytokine levels were on par with WT mice, while the 22KO mice displayed an increase of $CD8^+$ granzyme B (GZMB) production. Notably, the tumor-bearing dKO mice had significant increases of both interferon-γ (IFN-γ)– and GZMB-producing $CD8^+$ T cells in the spleens, and each cytokine was enhanced even in comparison to single KO animals (Fig. 5, B and C). Furthermore, both the 22KO and dKO mice had significant drops in Foxp3- and T_{reg}-suppressive marker MFI in peripheral T_{reg} cells, which was not observed in 21KO T_{reg} cells (Fig. 5, D to G). Collectively, these data suggest that the combined loss of *Usp22* and *Usp21* in T_{reg} cells results in enhanced activation of T_{eff} cell effect compared to individual loss of *Usp21* or *Usp22* alone.

Further analysis of tumor-infiltrating lymphocytes indicated a significant increase in $CD4^+$ and $CD8^+$ T cell frequencies in the dKO mice, with each compartment in the dKO secreting higher amounts of both IFN-γ and GZMB than WT mice (Fig. 5, H to J). Notably, the dKO mice had significantly higher levels of T_{eff} cell infiltration than both the 22KO and 21KO mice, as well as having the highest levels of IFN-γ secretion. Consistently, itT_{reg} cells in the 22KO and dKO mice had significantly lower T_{reg} infiltration and Foxp3 MFI than in the WT and 21KO mice (Fig. 5, K and L). Impairment in T_{reg}-suppressive functions, such as by *Usp22* and *Usp21* loss, perpetuates antitumor immunity by presumably alleviating T_{reg} suppression on cytotoxic $CD8^+$ T cells. The enhanced tumor rejection in the *Usp22* and *Usp21* dKO mice was largely abolished by antibody-induced CD8 depletion (Fig. 5M). Collectively, these data suggest that *Usp22* and *Usp21* cooperate to maintain T_{reg} cell function in the TME.

Identification of a *Usp22*-specific small-molecule inhibitor

Although our discovery that dual Usp inhibition delivers the strongest antitumor effect, *Usp22* presents as the dominant Foxp3-stabilizing Usp, and *Usp22* deletion alone was also sufficient in diminishing tumor burden. Responding consistently to TME factors, *Usp22* demonstrates potential as an antitumor immune therapeutic target. Therefore, we first aimed to identify *Usp22*-specific inhibitors. It has been suggested that in vitro purified *Usp22* protein lacks catalytic activity (*41*, *42*), leading to difficulties for high-throughput screening. Therefore, we used the computer-aided drug design (CADD) to develop a *Usp22*-specific small-molecule inhibitor (fig. S9A). As *Usp22* contains a highly conserved putative catalytic domain (Cys, His, and Asp) from yeast to human, a homology modeling study was performed to obtain a model of human *Usp22* for use in structure-based virtual screening (fig. S9B). Of three validated structural models of *Usp22*, the yeast UBP8 structure [Protein Data Bank (PDB) code 3MHS] was chosen as a template protein to construct the *Usp22* model by Swiss Model (*Usp22*-m) (fig. S9, C and D). To obtain conformation at the lowest potential, the structure of *Usp22*-m was further subjected to molecular dynamics (MD) simulation and clustering analysis using GROMACS 5.15, and the distance between Cys^{185} and His^{479} was increased from 3.6 to 4.8 Å in the position of catalytic site of *Usp22* (*Usp22*-md) (fig. S9, C and D). We further compared the predicted amino acid sequence of *Usp22* with 150 homologous full sequences. The conservation grades are mapped onto the structure and show that the Cys domain was highly conserved. This study provides not only the basis for the accuracy of homology modeling but also favorable conditions for drug selectivity screening.

We then used both Lipinski′s rule and Veber′s rule to filter through the Specs database and found a total of 240,000 compounds binding to the catalytic pocket of our *Usp22* model. We then filtered the top 100 compounds ranked by docking affinity by MD and molecular mechanics/Poisson-Boltzmann surface area (MM/PBSA) methods and were left with 25 compounds (table S1). This limited number of compounds allowed us for further biological screening. As *Usp22* suppression leads to marked reduction in Foxp3 expression levels, we used Foxp3 MFI reduction as a readout for the biological validation of *Usp22* inhibitory efficacy by each of the 25 chemicals. As indicated in table S1, the chemical S02 (11-anilino-7,8,9,10-tetrahydrobenzimidazo[1,2-b]isoquinoline-6-carbonitrile) showed strong efficacy in down-regulating Foxp3 expression. The compound S02, structure shown in Fig. 6A, bound stably in the *Usp22* catalytic domain pocket shown by the root mean square deviation (RMSD) trajectory (fig. S9E), with strong binding energies to our *Usp22*-md model (fig. S9F). Furthermore, analysis of S02 interaction with each residue of *Usp22* indicated that the side chain–negative residues (Glu and Asp) make a favorable contribution to the binding of the inhibitor and protein; however, the positively charged residues, such as Arg and Lys, play a detrimental role (fig. S9G). Therefore, this *Usp22* inhibitor stably bind not only to the hydrophobic residues but also to the charged and polar residues on the surface of the binding pocket of *Usp22* protein, implying its potent efficacy in suppressing *Usp22* catalytic functions.

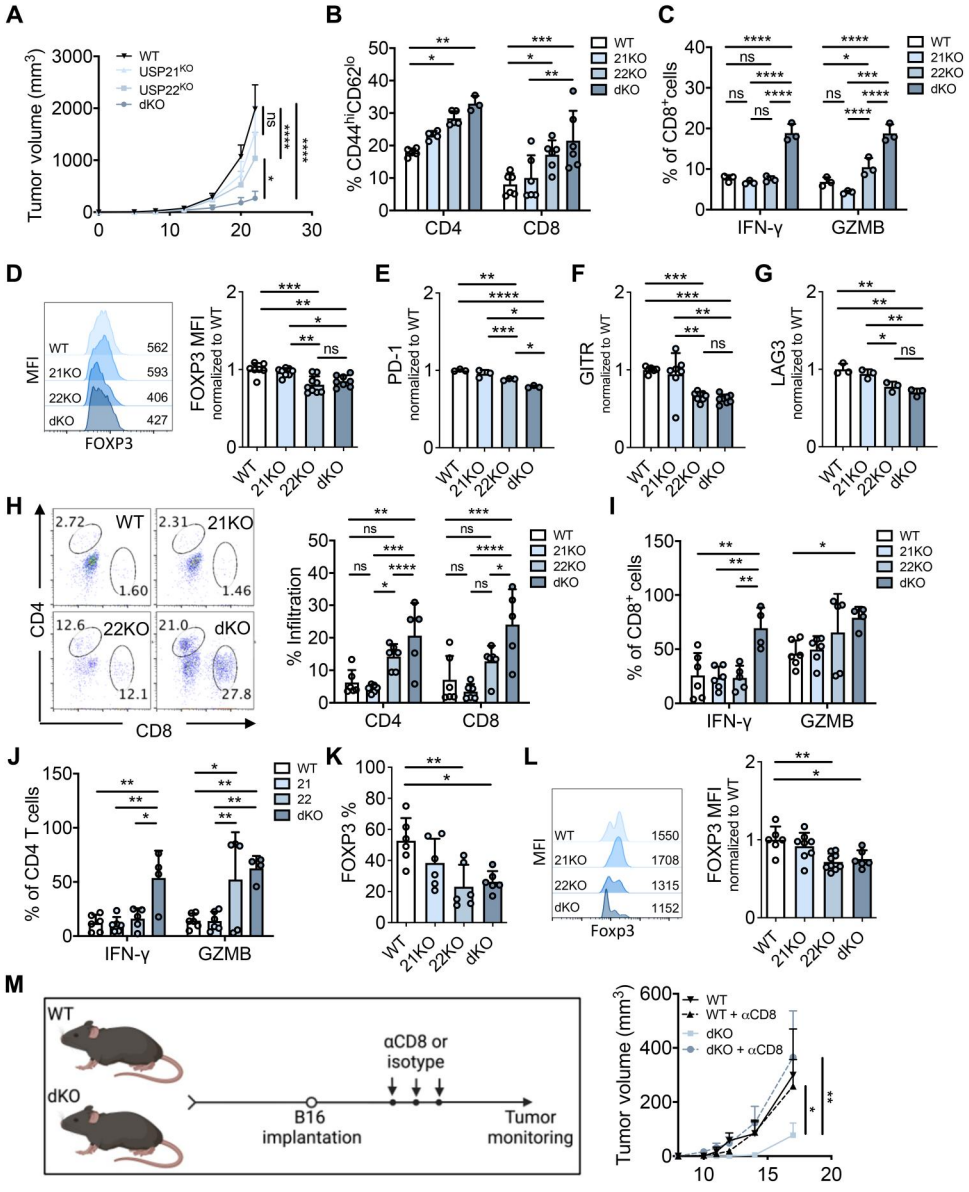

Fig. 5. Deletion of *Usp*22 and *Usp*21 in T_{reg} cells synergizes to enhance antitumor immunity. (**A**) Tumor growth curve of B16 cells subcutaneously injected in the flank of WT, 21KO, 22KO, and dKO mice (n = 13 to 14). (**B**) Percent activation as defined by $CD44^{hi}CD62L^{lo}$ of $CD4^+$ and $CD8^+$ T cells in the spleens of B16 challenged mice (n = 5 to 6). (**C**) Percent IFN-γ and GZMB production of peripheral $CD8^+$ T cells (n = 3). (**D**) Foxp3 MFI of peripheral T_{reg} cells relative to WT (n = 7 to 9). (**E**) PD-1 MFI of peripheral T_{reg} cells relative to WT (n = 3). (**F**) GITR MFI of peripheral T_{reg} cells relative to WT (n = 6 to 8). (**G**) LAG3 MFI of peripheral T_{reg} cells relative to WT (n = 3). (**H**) Representative flow cytometry plot and graphical representation of % infiltration of $CD4^+$ and $CD8^+$ T cells within the tumor (n = 5 to 6). (**I** and **J**) Percentage IFN-γ and GZMB production of intratumoral $CD8^+$ and $CD4^+$ cells (n = 5 to 6). (**K**) Representative $Foxp3^+$ percentage of $CD4^+$ cells relative to WT in itT_{reg} cells (n = 6). (**L**) Representative flow plot (left) and quantitative representation of Foxp3 MFI within tumor T_{reg} cells relative to WT (n = 6 to 9). (**M**) CD8 T cell depletion on B16 tumor growth in WT and dKO mice (n = 3 to 4). (A to C, H to J, and M) Two-way ANOVA with multiple comparisons between rows was performed to determine statistical significance. All data are presented as means ± SD. *P < 0.05, **P < 0.01, ***P < 0.001, and ****P < 0.0001. (D to G, K, and L) One-way ANOVA with multiple comparisons between rows was performed to determine statistical significance. All data are presented as means ± SD. *P < 0.05, **P < 0.01, ***P < 0.001, and ****P < 0.0001.

Usp22i-S02 down-regulates FoxP3 in a *Usp22*- but not *Usp21*-dependent manner

We then determined the dose response of compound S02, now dubbed Usp22i-S02, in both WT and *Usp22*-null iT_{reg} cells (Fig. 6, A and B, and fig. S10, A and B). At a concentration of 10 μg/ml, Usp22i-S02 decreased Foxp3 MFI to a level comparable in *Usp22*-null iT_{reg} cells with little effect on viability, indicating a near-complete suppression of *Usp22* activity in stabilizing Foxp3 (fig. S10A). The effect of Usp22i-S02 on Foxp3 was further confirmed by Western blot (fig. S10C). Lower doses of Usp22i-S02 administration to human T_{reg} cells significantly decreased Foxp3 MFI with little effect to cell viability, showing the relevance of this inhibitor to human cells (fig. S10, D to F). In contrast, Usp22i-S02 had minimal effect on Foxp3 levels in murine T_{reg} cells already lacking

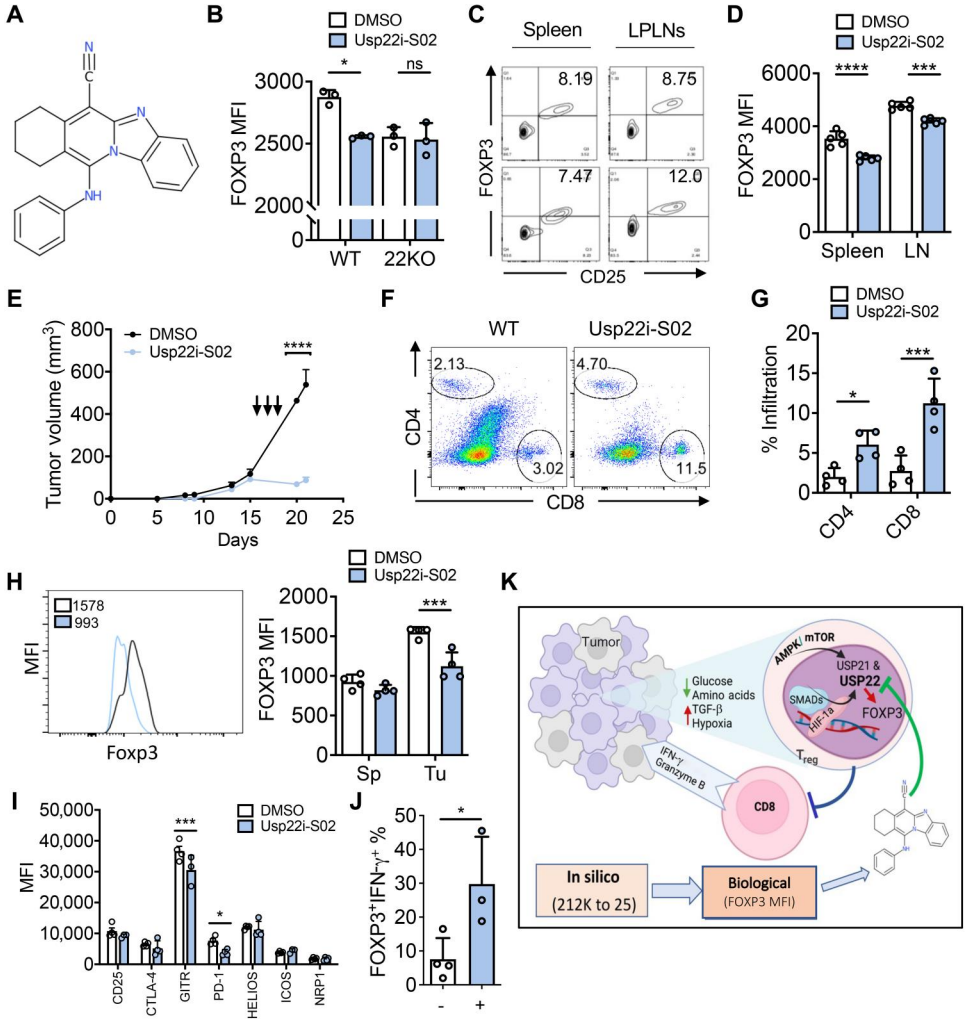

Fig. 6. *Usp22* inhibitor administration enhances antitumor immunity. (**A**) Structure of compound CS30 (Usp22i-S02). (**B**) Foxp3 MFI in WT and 22KO of T_{reg} cells after treatment with Usp22i-S02 (20 μg/kg) in vivo ($n = 3$). (**C**) Representative flow cytometry plot of $Foxp3^+CD25^+$ MFI of $CD4^+$ peripheral cells of mice treated with Usp22i-S02 (20 μg/kg) relative to control ($n = 5$). (**D**) Graphical representation of Foxp3 MFI upon Usp22i-S02 administration ($n = 5$). (**E**) Tumor growth curve of LLC1 cells subcutaneously injected in the flank of WT mice with or without the addition of the Usp22 inhibitor (20 mg/kg per time) starting at day 15 in 100 μl of oil ($n = 4$). (**F** and **G**) Representative flow cytometry plot and graphical representation of % infiltration of $CD4^+$ and $CD8^+$ T cells within the tumor ($n = 4$). (**H**) Representative histogram plot and graphical representation of itT_{reg} Foxp3 MFI ($n = 4$). (**I**) MFI of itT_{reg}-suppressive markers ($n = 3$ to 4). (**J**) Percent $Foxp3^+IFN\text{-}\gamma^+$ itT_{reg} cells in control and Usp22-S02–treated mice ($n = 3$ to 4). (**K**) Proposed model: TME-specific factors can drive increased levels of Usp22 and Usp21 potentially through modulation of TGF-β signaling, HIF1-α, AMPK, and mTOR activity to render T_{reg} cells more stable in the tumor microenvironment. (D, E, and G to I) Two-way ANOVA with multiple comparisons between rows was performed to determine statistical significance. (J) Unpaired two-tailed *t* test was performed to determine significance. All data are presented as means ± SD. $^*P < 0.05$, $^{**}P < 0.01$, $^{***}P < 0.001$, and $^{****}P < 0.0001$.

Usp22 both in vivo and in vitro (Fig. 6, B to D) while having full effect on T_{reg} cells lacking *Usp21* (fig. S10G). Functionally, Usp22i-S02 administration had similar effects to *Usp22* deletion in T_{reg} cells, resulting in enhanced Foxp3 degradation, increased Foxp3 ubiquitination, and decreased Foxp3 transcription (fig. S10, H to J). Furthermore, Usp22i-S02–mediated Foxp3 degradation was halted by MG132 protease inhibition, indicating that Usp22i-S02 enhances proteasomal-specific degradation of Foxp3 (fig. S10K). Therefore, these results indicate that Usp22i-S02 is a potent *Usp22*-specific small-molecule inhibitor that down-regulates Foxp3 expression in T_{reg} cells in a *Usp22*- but not *Usp21*-dependent manner.

Usp22i-S02 administration enhances antitumor immunity with low toxicity in mice

An important aspect of a potential immunotherapeutic is its antitumor functionality paired with low immune toxicity. We used the LLC1 Lewis lung carcinoma syngeneic tumor model to test the efficacy of Usp22i-S02 in enhancing antitumor immunity. Upon LLC1 challenge, WT mice administered Usp22i-S02 at 20 mg/kg for 5 days showed a marked reduction in tumor volume and weight compared to untreated mice (fig. S11, A and B). As expected, Usp22i-S02 treatment resulted in a significant increase in $CD8^+$ T cell tumor infiltration (fig. S11, C and D). Further analysis of tumor-infiltrating lymphocytes indicated a less exhausted phenotype in $CD8^+$ T cells, with an increase in $CD44^+$ cells and a decrease

in T-bet$^+$, Blimp1$^+$, and annexin V$^+$ cells (fig. S11, E to H). Like in the T_{reg}-specific *Usp22* KO mice, intratumoral Foxp3$^+$ T_{reg} percentage significantly decreased following administration of Usp22i-S02 (fig. S11I). Therefore, specifically targeting *Usp22* with a small-molecule inhibitor enhances antitumor immunity with the potential to complement existing immunotherapies.

As tumor rejection may be due to Usp22i-S02 toxicity or non–T_{reg}-specific immune cell modulation, we determined its effects in naïve mice. We found little alteration in the body weights, B cell and T_{eff} cell percentages and proliferation, and T_{eff} cell activation of treated mice at 20 mg/kg body weight compared to dimethyl sulfoxide (DMSO)–treated controls (fig. S11, J to M). Unlike T_{eff} cells, T_{reg} cell death was significantly increased (fig. S11N), resulting in a decrease in T_{reg} percentage (fig. S11K). T_{reg} proliferation was also increased (fig. S11L), potentially indicating a dysfunctional effector T_{reg} (eT_{reg}) population by Usp22i-S02 treatment. Furthermore, a comprehensive tissue panel showed no pancreatic, liver, or kidney organ toxicity form Usp22i-S02–treated mice (fig. S11, O to Q). These data indicate that administration of Usp22i-S02 results in a T_{reg}-specific phenotype in naïve mice with little effects on other immune cell types and tissue toxicity.

Usp22i-S02 holds great therapeutic efficacy in treatment of the preestablished tumor

To further evaluate the efficacy of Usp22i-S02 in antitumor immunotherapy at a clinically relevant setting, we tested the inhibitor on established tumors. Following initial LLC1 tumor establishment 15 days after tumor cell implantation, mice administered Usp22i-S02 at 20 mg/kg for 3 days showed marked tumor rejection compared to untreated mice (Fig. 6E). Analysis of tumor-infiltrated immune cells revealed a significant increase in both CD4 and CD8 T_{eff} cell tumor infiltration (Fig. 6, F and G). Foxp3 MFI levels in the intratumoral, but not splenic, T_{reg} cells were significantly decreased following administration of Usp22i-S02 (Fig. 6H). Consequently, itT_{reg} cells had lower levels of GITR and PD-1 and expressed significantly higher levels of IFN-γ (Fig. 6, I and J). Our data indicate that Usp22i-S02 treatment partially impairs the suppressive functions of T_{reg} cells specifically within the tumor, potentially leading to T_{reg} dysfunction and fragility (*40*). Therefore, Usp22i-S02 holds great potential as an antitumor immunotherapy at a clinically relevant setting.

As *Usp22* is also an important oncogene (*43*, *44*), we were interested in the potential dual-therapeutic function of Usp22i-S02. Administration of Usp22i-S02 to LLC1 cells in vitro resulted in decreased tumor cell counts, viability, and growth (fig. S12, A to C). Furthermore, treatment of $Rag^{-/-}$ mice with established tumors resulted in slight but significant tumor rejection (fig. S12D). Together, our data show the critical role of *Usp22* in T_{reg} cell stability and adaptation within the TME, and that specifically targeting *Usp22* with a small-molecule inhibitor not only enhances antitumor immunity but also has a dual role as a chemotherapeutic agent.

Collectively, our study illustrates a previously unappreciated role of Foxp3-specific DUBs, *Usp22* and *Usp21*, as environmentally sensitive factors that enhance Foxp3 stability in the TME. We identified several TME factors that up-regulate *Usp22* and *Usp21*, ultimately stabilizing Foxp3: (i) tumor-secreted TGF-β, (ii) hypoxia, (iii) glucose restriction, and (iv) amino acid deprivation (Fig. 6K). These findings unveil new mechanisms behind the metabolic and functional uniqueness of itT_{reg} cells, providing evidence on how these cells adapt in response to environmental cues within solid tumor to support their function. In addition to our previous work demonstrating that loss of *Usp22* in the T cell compartment results in only a T_{reg}-specific impairment (*15*), our data provide a rationale for *Usp22*-targeted therapy to enhance antitumor immunity. Last, our novel *Usp22* inhibitor, Usp22i-S02, successfully reduced tumor burden in a T_{reg}-specific manner (Fig. 6K).

DISCUSSION

Emerging data suggest that the TME, often deprived of nutrients and oxygen, likely offers a metabolic advantage to T_{reg} cells over T_{eff} cells, further promoting an immunosuppressive microenvironment. However, the TME-specific factors and their cellular targets that potentiate T_{reg} cell–suppressive function and adaptation remain largely unidentified.

It has been well documented that itT_{reg} cells are more suppressive and often have high Foxp3 expression (*7*, *8*, *45*), and we first confirmed these results in various murine tumor models. Our findings that itT_{reg} levels of *Usp22*, and occasionally *Usp21*, are up-regulated in these models concurrently with Foxp3 suggest that TME factors selectively induce these USPs to stabilize Foxp3 expression. We observed increased *Usp22* levels in correlation with Foxp3 in human itT_{reg} cells, broadening the relevance of this pathway to human tumors. Although *Usp7* in T_{reg} cells is known to control Foxp3 expression and T_{reg}-suppressive function in a model of colitis, we did not observe an increase in *Usp7* expression in itT_{reg} cells, suggesting that *Usp7* may primarily regulate T_{reg} function during homeostatic conditions.

TGF-β is a major player in iT_{reg} conversion and stability and is broadly secreted by many tumor types. We found that tumor-secreted TGF-β is sufficient in up-regulating *Usp22* through canonical TGF-β signaling and *Usp21* through noncanonical signaling. Furthermore, *Usp22* partakes in a feedback loop to further up-regulate itself and Foxp3 through SMAD protein stabilization. The complexity of the p38 and MAPK pathway offers wide-ranging possibilities for downstream regulation of *Usp21*. p38 stabilizes GATA3 and STAT3 (signal transducer and activator of transcription 3), potentially leading to downstream *Usp21* up-regulation (*46*–*50*). As TGF-β is widely implicated in Foxp3 expression and stability and iT_{reg} function, our data add a new level of complexity to already known systems (*19*, *51*). These novel mechanisms potentially function to ensure T_{reg} cell stabilization through alternate pathways, strengthening their ability to maintain their suppressive capacity in diverse environments.

However, tumor-secreted TGF-β is not the only factor capable of up-regulating USPs, because T_{reg} cells treated with EG7 TCM could not recapitulate the increase of *Usp22* seen in itT_{reg} cells isolated from EG7 tumors. Therefore, we hypothesized that other environmental factors within the TME are also implicated in T_{reg} stabilization through USPs. As hypoxia is a major hallmark of solid tumors (*3*, *25*), we investigated how low oxygen conditions influence *Usp22* levels in T_{reg} cells. Our findings that hypoxia induced *Usp22* in a HIF-dependent manner, and loss of *Usp22* resulted in diminished Foxp3 stability, imply that hypoxia can stabilize T_{reg} cells through *Usp22*-mediated Foxp3 stabilization. Our conclusion is in line with previous data that demonstrate heightened proliferation and suppressive capabilities of T_{reg} cells under hypoxic conditions and

is strengthened by the two active HIF binding sites along the *Usp22* promoter (*23*).

Along with a decrease in oxygen availability, the competition for nutrients that occurs within the TME influences immune cell growth, survival, and function. Classically, T_{reg} cells are thought to have a significantly lower reliance on glycolysis than T_{eff} cells, potentially providing another advantage in the TME (*4*, *30*, *33*). Our data identify *Usp22* and, to a lesser extent, *Usp21* as important mediators in this process, functioning to stabilize Foxp3 under glucose and amino acid deprivation. Nutrient deprivation in T cells is generally accompanied by a shift toward oxidative metabolism following AMPK activation and mTOR inhibition, and the balance of AMPK and mTOR signaling functions as an environmental sensor for nutrient availability (*31*, *52*). Foxp3 stabilization, in part, appears secondary to this metabolic shift (*37*, *53*). As protein translation is severely reduced under cellular nutrient deprivation, our data revealing mTOR inhibition as a major player in *Usp22* and *Usp21* up-regulation describe a potential mechanism by which T_{reg} cells stabilize important proteins through targeted up-regulation of deubiquitinases. By up-regulating Foxp3-specific deubiquitinases *Usp22* and *Usp21*, T_{reg} cells enhance their function, stability, and survival under energy stress.

The metabolic status of an immune cell is highly important within the TME for their cell survival and function. As T_{reg} cells can adapt to low-oxygen, low-nutrient environments, they have a metabolic advantage compared to T_{eff} cells. Foxp3 is essential to this process as it is known to promote oxidative phosphorylation within T_{reg} cells. We show that *Usp22*- and *Usp21*-deficient T_{reg} cells have significantly altered expression of metabolic genes and impaired OCR and ECAR. In addition, RNA sequencing analysis demonstrated that the loss of *Usp22* and *Usp21* in T_{reg} cells resulted in the up-regulation of multiple pathways associated with cell growth and proliferation. Collectively, these data raise the intriguing possibility that *Usp22* and *Usp21* work to promote T_{reg} cell fitness in nutrient-restricted environments in part by modulating T_{reg} cell metabolic programs through Foxp3 stabilization. Ultimately, our data indicate that microenvironmental stress within the TME up-regulates T_{reg} USP levels, which then function to stabilize Foxp3. Enhanced Foxp3 stability further supports T_{reg} cell adaptation to the TME, thus identifying *Usp22* and *Usp21* as important environment-sensitive factors that regulate T_{reg} cell identity, metabolism, and function in the TME.

As loss of *Usp22* in T_{reg} cells resulted in enhanced antitumor immunity relative to the loss of *Usp21*, there is a suggested dominance of *Usp22* in itT_{reg} cells. Therefore, specifically targeting *Usp22* may be sufficient in eliminating the advantage T_{reg} cells have over T_{eff} within the TME. To test this, we developed and tested the first ever *Usp22*-specific inhibitor. Administration of the inhibitor resulted in a marked decrease in itT_{reg} number, resulting in strong in vivo antitumor effects.

In addition, we and others have demonstrated that *Usp22* is up-regulated in many cancer types, such as gastric carcinoma, pancreatic cancer, and melanoma, and has been correlated with poor prognosis (*54*). *Usp22* promotes oncogenic c-Myc activation as well as indirectly antagonizes the tumor-suppressive function of p53, and clearly diminishes tumor growth in in vitro and in vivo LLC1 models (*55*). *Usp22* also functions to maintain Foxp3 expression through DUB function at the transcriptional and posttranslational levels. This duality makes *Usp22* highly attractive potential therapeutics that can target both tumor cell–intrinsic and immunosuppressive pathways simultaneously. Our data demonstrate that *Usp22* is a targetable protein and that the inhibitor Usp22i-S02 has the potential of being incorporated into tumor immune therapies.

As approaches to specifically inhibiting T_{reg}-suppressive functions are yet to be identified, our discovery that *Usp22* deletion impairs itT_{reg}-suppressive activity without promoting extensive inflammatory response indicates that *Usp22* inhibition holds a great therapeutic potential in antitumor immune therapy. To enhance the effects of immunomodulatory therapies, minimizing the heightened suppression by itT_{reg} cells through *Usp22* targeting while concurrently enhancing T_{eff} antitumor immunity through dual therapeutics could significantly increase response rates and overall survival across cancer types.

MATERIALS AND METHODS

Animal strains

Usp22$^{fl/fl}$FoxP3$^{YFP\text{-}Cre}$ mice were generated previously as described (*14*). Frozen sperm of C57BL/6N-A^{tm1Brd}*Usp21*$^{tm1a(EUCOMM)Wtsi/WtsiBait}$ were purchased form Emma Mouse Repository (EMMA ID: 07280). Blastocyst injections resulted in several chimeric mice with the capacity for germline transmission. T_{reg}-specific *Usp21*-null mice were generated by breeding *Usp21*$^{fl/fl}$ mice with *Foxp3*$^{YFP\text{-}cre}$ mice (obtained from The Jackson Laboratory). *Usp22*$^{fl/fl}$*Usp21*$^{fl/fl}$FoxP3$^{YFP\text{-}Cre}$ mice were generated by breeding *Usp22*$^{fl/fl}$FoxP3$^{YFP\text{-}Cre}$ with *Usp21*$^{fl/fl}$FoxP3$^{YFP\text{-}Cre}$. This breeding strategy produced the T_{reg}-specific KO of *Usp22* (*Usp22*^{KO}) and *Usp21* (*Usp21*^{KO}) and a dKO of both. These mice were maintained and used at the Northwestern University mouse facility under pathogen-free conditions in accordance with institutional guidelines and following animal study proposals approved by the institutional animal care and use committees (IACUCs). Unless stated otherwise, all figures are representative of experiments with 6- to 8-week-old mice. All animal experiments followed IACUC protocols: IS00001629 and IS00015611.

Syngeneic tumor models

EG7 lymphoma, LLC1 lung carcinoma, and B16-F10 melanoma cell lines were provided by the Zhang laboratory at Northwestern and used for tumor models as previously reported (*14*). The cell lines were cultured in Dulbecco's modified Eagle's medium (DMEM) with 10% fetal bovine serum (FBS) and were tested for mycoplasma using a LookOut Mycoplasma PCR detection kit (Sigma-Aldrich, MP0035-1KT). Cultured cancer cells were trypsinized and washed once with phosphate-buffered saline (PBS). LLC1 lung carcinoma tumor cells were subcutaneously administered to the right flank of 8- to 10-week-old mice at 1×10^6 tumor cells per mouse, and B16 melanoma at 5×10^4 tumor cells per mouse. Tumors were measured every 2 to 3 days by measuring along three orthogonal axes (*x*, *y*, and *z*), and tumor volume was calculated as (*xyz*)/2. The tumor size limit agreed by the Institutional Review Board (IRB) was 2 cm^3. Mice were intraperitoneally treated with anti-CD8 (Bio X Cell, 53-6.72) or isotype (Bio X Cell, 2A3) (200 mg) every 3 days starting on day 5.

In vitro iT_{reg} cell generation

Splenic $CD4^+CD25^-CD44^-CD62L^+$ naïve T cells were isolated using a mouse naïve CD4 isolation kit (STEMCELL Technologies, catalog no.19765) and cultured in 24-well plates at 5×10^5 cells per well for 3 days. Cells were cultured in T cell medium made of complete RPMI 1640 medium containing 10% FBS, 1% penicillin/streptomycin (MediaTech), 50 μM β-mercaptoethanol (Gibco), and 1% L-glutamine (Gibco). Wells were coated in anti-CD3 (3 μg/ml) and anti-CD28 (5 μg/ml) antibodies. Culture medium was supplemented with interleukin-5 (IL-2) (5 ng/ml), anti–IFN-γ (2 μg/ml), anti–IL-4 (2 μg/ml), and TGF-β (5 ng/ml) (unless otherwise stated), all purchased from PeproTech.

Ex vivo nT_{reg} cell culture conditions

nT_{reg} cells were isolated from mouse spleens using a $CD4^+$ T cell negative isolation kit (STEMCELL Technologies, catalog no.17952), followed by yellow fluorescent protein–positive (YFP^+) flow cytometry sorting on FACSAria (BD Biosciences) at 99% efficiency. Cells were then plated in a 96-well plate at 1×10^5 cells per well with 2000 U of IL-2 and CD3/CD28 beads (from a T_{reg} expansion kit, Miltenyi Biotec, catalog no.130-095-925) and added to T cell medium following the manufacturer's instructions.

In vitro iT_{reg} cell TCM and TGF-β assays

Previously generated iT_{reg} cells were washed and rested for 7 hours in Opti-MEM containing IL-2 (5 ng/ml) to maintain survival. Opti-MEM was used to avoid any TGF-β contamination found in serum. After resting, the cells were incubated in Opti-MEM containing IL-2 with or without the addition of TGF-β (20 ng/ml) or the various tumor cell media (B16, LLC1, and EG7). TCM was obtained by plating B16, EG7, or LLC1 cell lines at 50% confluency for 16 hours. TCM was then mixed 50:50 with fresh Opti-MEM and incubated on iT_{reg} cells for 24 hours. The TGF-β inhibitor LY 3200882 (MedChem Express, catalog no. HY-103021) was added at 25 μg/ml where indicated.

In vitro T_{reg} cell hypoxia culture

nT_{reg} cells were isolated as described above and cultured at 37°C under a normoxic (21% O_2) or hypoxic condition (1% O_2) for 24 hours. Hypoxia was induced using the O_2 Control InVitro Glove Box from Coy Laboratory Products. T cell medium was incubated at 37°C at normoxia or hypoxia for 3 hours before use. Cells were then collected, and RNA was extracted as described above. For iT_{reg} cells, cells were isolated and polarized as described above. Subsequently, cells were rested in Opti-MEM overnight and then plated in Opti-MEM containing IL-2 (5 ng/ml) under a normoxic or hypoxic condition. Opti-MEM was incubated at 37°C at normoxia or hypoxia overnight before use. Hypoxia stability assay was conducted as described above, but cells were cultured in normoxia or hypoxia for 72 hours, then collected, and stained for Foxp3 for flow cytometry.

Glucose and amino acid restriction assays

nT_{reg} cells were isolated as described above and cultured in either normal T cell medium, T cell medium lacking glucose (Thermo Fisher Scientific, catalog no. 11879020), or T cell medium lacking amino acids including glutamine (US Biological, catalog no. R9010-02) substituted with dialyzed FBS (Gibco, catalog no. A3382001) for 24 hours at 1×10^5 cells per well. T cell medium included 2000 U of IL-2 and CD3/CD28 beads as described above. iT_{reg} cells were isolated and polarized as described above for 3 days. Following polarization, iT_{reg} cells were cultured in normal T cell medium or T cell medium lacking glucose or amino acids for 24 hours. Both nT_{reg} and iT_{reg} cells were then collected, and RNA was extracted as described above. For stability assays, cells were cultured as described above for 48 hours, then collected, and stained for Foxp3 for flow cytometry.

Cell isolation and flow cytometry for analysis of splenic and intratumoral T_{reg} cells

T cells were isolated from mouse spleen using a $CD4^+$ T cell negative isolation kit (STEMCELL Technologies, catalog no.17952) per the manufacturer's instructions. To isolate murine and human tumor-infiltrating lymphocytes, subcutaneous tumors were cut into small fragments and digested by collagenase D (Sigma-Aldrich) and deoxyribonuclease (DNase) (Sigma-Aldrich) for 1 hour at room temperature before isolation with a $CD45^+$ positive selection kit (STEMCELL Technologies, catalog no. 100-0350). Murine-enriched cells were further sorted for YFP^+ ($Foxp3^+$) using FACSAria (BD Biosciences). Human-enriched cells were further sorted for $CD4^+CD25^+CD127^-$ cells. Purity of sorted cells was >99%. Flow cytometry analysis of cells was done using FACSCanto II. Samples were initially incubated with CD16/32 antibodies to block antibody binding to Fc receptor. Single-cell suspensions were stained with relevant antibodies (table S2) and subsequently washed twice with cold PBS containing 3% FBS. For intracellular staining, cells were fixed, permeabilized, and stained for transcription factors using the Foxp3 Transcription Factor Staining Buffer Set (eBioscience, 00-5523-00) following the manufacturer's instructions. For cytokine staining, cells were first stimulated for 4 to 5 hours with phorbol 12-myristate 13-acetate (PMA; 20 ng/ml) plus 0.5 μM ionomycin (Sigma-Aldrich) in the presence of monensin (10 μg/ml) (eBioscience) before staining. Data were analyzed with FlowJo software.

Cell lines, plasmids, antibodies, and reagents

Human embryonic kidney (HEK) 293 cells were purchased from the American Type Culture Collection (ATCC) and stored in the Fang laboratory. EG7 Lymphoma, LLC1 lung carcinoma, and B16-F10 melanoma cell lines were provided by the Zhang laboratory at Northwestern and used for tumor models as previously reported (*14*). The cell lines were cultured in DMEM with 10% FBS and were tested for mycoplasma using a LookOut Mycoplasma PCR detection kit (Sigma-Aldrich, MP0035-1KT). MYC-*Usp22*, Flag-*Smad2*, Flag-*Smad3*, Flag-*Smad4*, and hemagglutinin (HA)–ubiquitin pCMV expression plasmids and their tagged vectors were constructed by the Fang laboratory and stored at −20°C. All Western blot, coimmunoprecipitation, and flow cytometry antibodies are listed in table S2. PMA, ionomycin, and cycloheximide were purchased from Sigma-Aldrich. Monensin was purchased from eBioscience. Antibodies are listed in table S2.

RNA extraction for RNA sequencing and qPCR

RNA was extracted using the RNeasy Micro Kit (Qiagen, catalog no. 74004) from sorted $Foxp3^+$ (YFP^+) T_{reg} cells from mouse organs. qPCR was performed following the manufacturer's protocol using gene-specific primer sets (table S3). RNA sequencing was

performed by the Northwestern RNA sequencing core. Elaboration is found in the Supplementary Materials.

RNA sequencing and qPCR analysis

RNA was extracted using the RNeasy Micro Kit (Qiagen, catalog no. 74004) from sorted Foxp3$^+$ (YFP$^+$) T_{reg} cells from mouse organs. qPCR was performed following the manufacturer's protocol using gene-specific primer sets (table S3). Real-time PCR data were analyzed using the $\Delta\Delta C_t$ method with actin as the housekeeping gene. Gene expression was normalized to WT, untreated T_{reg} cells unless otherwise noted. RNA sequencing was performed by the Northwestern RNA sequencing core. The quality of DNA reads, in fastq format, was evaluated using FastQC. Adapters were trimmed, and reads of poor quality or those aligning to ribosomal RNA (rRNA) sequences were filtered. The cleaned reads were aligned to the *Mus musculus* genome (mm10) using STAR (*56*). Read counts for each gene were calculated using htseq-count (*57*) in conjunction with a gene annotation file for mm10 obtained from UCSC (University of California Santa Cruz; http://genome.ucsc.edu). Differential expression was determined using edgeR (*58*, *59*). The cutoff for determining significantly differentially expressed genes was a false discovery rate (FDR)–adjusted *P* value of less than 0.05. Following differential expression analysis, GSEA was performed using GSEA v4.03 (https://pubmed.ncbi.nlm.nih.gov/16199517/). For each separate KO mouse (*Usp21*, *Usp22*, and dKO), an inclusion cutoff of FDR-adjusted *P* value of <0.01 was set. Lists of genes, ordered by $\log_2$(fold change), were then run with the GSEA preranked tool under standard parameters against the Hallmarks MSigDB 7.2 gene sets (www.ncbi.nlm.nih.gov/pmc/articles/PMC4707969/). Normalized enrichment scores were then plotted for gene sets enriched at an FDR *q* value of <0.25.

ChIP-qPCR sample preparation

iT_{reg} cells (as described above) were used for immunoprecipitation to allow for ample cell number. Three million iT_{reg} cells per immunoprecipitation were fixed in 37% formaldehyde for 10 min at 37°C. Glycine was then added to a final concentration of 0.125 M, and the samples were incubated for an additional 5 min at room temperature. The cells were subsequently washed with ice-cold PBS with 1× protease inhibitor cocktail (Roche, catalog no. 36363600). The ChIP assay was done using the Millipore ChIP Assay Kit (lot no. 3154126) following the protocol as described previously (*14*).

Immunoprecipitation and Western blots

Coimmunoprecipitation and Western blots were performed as previously described (*14*). For overexpression, plasmids were transfected into HEK293 (ATCC) cells for 24 hours before being resuspended in radioimmunoprecipitation assay (RIPA) buffer with 1× protease inhibitor cocktail. Primary cells were collected and directly resuspended in RIPA buffer with 1× protease inhibitor cocktail. Antibodies and plasmids used are listed in table S2. Membranes were then developed with enhanced chemiluminescence. The relative protein expression levels were quantified using Bio-Rad Image software and normalized with the loading controls unless otherwise noted.

Ubiquitination assay

For overexpression, Flag-Smad proteins and HA-ubiquitin plasmids were cotransfected into HEK293 cells using TurboFect Transfection Reagent (Thermo Fisher Scientific, R0532) along with either Myc empty vector or Myc-*Usp22*. After 24 hours, the cells were collected and immunoprecipitated with anti-Flag to pull down the relevant SMAD antibody and immunoblotted for HA-ubiquitin to assess SMAD protein ubiquitination in the presence or absence of functional *Usp22*. Whole-cell lysate controls were immunoblotted with horseradish peroxidase (HRP)–conjugated Myc and HRP-conjugated Flag to show transfection efficiency. For endogenous ubiquitination assay, iT_{reg} cells were cultured as previously described, and cells were directly used for the assay. Either ubiquitin or Foxp3 antibodies were used for immunoprecipitation.

Assessment of cellular metabolism

The rates of mitochondrial oxygen consumption and glycolysis were measured using the Seahorse XF-96 analyzer (Agilent). Splenic T_{reg} cells (YFP$^+$) (250,000) were isolated by flow sorting and adhered to XF96 cell culture plates using Cell-Tak (Corning) per the manufacturer's instructions. Cells were plated in XF RPMI medium (Agilent) supplemented with 1% FBS, 11 mM glucose, 2 mM glutamine, and 1 mM pyruvate to match normal concentrations of those metabolites in base RPMI. The basal mitochondrial OCR was determined by subtracting the antimycin A– and piericidin A–sensitive oxygen consumption from the basal mitochondrial oxygen consumption. The basal glycolytic rate was calculated by subtracting the 2-deoxyglucose–sensitive ECAR from the basal ECAR. Antimycin A and piericidin A purchased from Sigma-Aldrich were both used at a final concentration of 1 μM. 2-Deoxyglucose purchased from Sigma-Aldrich was used at a final concentration of 25 mM.

Homology modeling of human Usp22

The amino acid sequence of human *Usp22* was retrieved from the sequence database of UniProt (www.uniprot.org/uniprot/ UniProt ID: Q9UPT9). UBP8 structure (PDB code 3MHS) was chosen as a template protein to construct the human *Usp22* model. The homology modeling of the human *Usp22* model was performed by three different homology modeling programs including SWISS MODEL, I-TASSER, and MODELLER. Subsequently, the quality of the *Usp22* models was checked with structure validation programs including PROCHECK and Verify_3D programs. Last, the best model was subjected to energy minimization for removing clashes between side chains using GROMACS 5.1.5 and subsequently applied in structure-based virtual screening.

Virtual screening

Specs (www.specs.net) database containing 212,558 compounds was first filtered by lead-like properties ($180 < MW < 480$, $-0.5 < ClogP < 5.5$, $PSA < 140$ Å, $0 <$ rotational bonds < 10, $0 <$ donor and acceptor < 13) (MW=molecular weight; PSA=polar surface area) and led to a total of 102,442 compounds using DruLiTo software. The three-dimensional geometry of the ligands was optimized, minimized, and prepared using Open Babel. The virtual screening was performed using AutoDock Vina program. The docking grid was created with the grid points 16, 18, and 16 and defined as coordinates of the center of binding site with 37.64, 11.33, and 70.33 for *x*, *y*, and *z* dimensions, respectively. The Genetic Algorithms were selected to perform the molecular docking and keeping other docking parameters in default. The

top 100 compounds ranked by docking affinity were selected for further study. Moreover, residual interactions at the protein-drug interface were evaluated using LigPlot.

Molecular docking mechanism

Molecular docking result showed that compound S02 stably binds in the *Usp22* catalytic domain pocket, mainly in the hydrophobic effect provided by the amino acid residues His^{471}, Gln^{261}, Gly^{478}, Glu^{476}, Leu^{475}, Asp^{262}, Arg^{419}, Tyr^{480}, and Phe^{412}. It is worth noting that not only the benzene ring on compound S02 forms a hydrophobic interaction with the Tyr^{480} residue but also the hydrogen atom on the anilino group of ligand acts as hydrogen donor to form a hydrogen bond with the hydrogen acceptor on the Tyr^{480} residue. Binding stability indicates that the anilino functional group may play an important role in the inhibitory activity of *Usp22* (Fig. 1D).

MD simulation

The conformation of the complexes formed between ligands and *Usp22* receptor protein was predicted using AutoDock Vina program, and all of the MD simulations were performed by GROMACS 5.1.5 with Amber99sb force field. After MD simulation, the molecular mechanics energies combined with the MM/PBSA methods were used to calculate the binding free energy of ligands with *Usp22* receptor protein. Structural stability of complexes was compared by analyzing RMSD and the hydrogen-bonding interactions throughout the trajectory.

In vitro inhibitor assays

All nT_{reg} and iT_{reg} cells were plated as described above. dMOG (Sigma-Aldrich, catalog no. D3695) was administered to the cells in relevant experiments at 1 mM for 24 hours. Oligomycin (Sigma-Aldrich, catalog no. 75351) was administered at 1 μM to the medium of the cells in relevant experiments for 24 hours. AICAR (Sigma-Aldrich, catalog no. 52871) was administered to relevant cells for 24 hours. Torin1 (Millipore, catalog no. 475991) was administered to the relevant cells at 250 nM for 24 hours. Foxp3 protein level was assessed via flow cytometry following 48 hours of treatment of inhibitors described above. In vitro administration of Usp22i-S02 was at 10 μg/ml.

Usp22i-S02 in vivo inhibitor experiments

LLC1 cells were transplanted into 6- to 8-week-old C57BL/6 or $RAG^{-/-}$ male mice. Subcutaneous injections were performed in the right flank of mice in a final volume of 100 μl using 1×10^6 cells per injection. The Usp22i-S02 was injected intraperitoneally at a concentration of 20 mg/kg per time, in 100 μl of oil, twice a day for 3 to 5 days beginning on either the first day of the LLC1 cell injection or when tumors reached 100 mm^3. Control animals received 100 μl of oil alone. Subcutaneous tumor diameters were measured daily with calipers until any tumor in the mouse cohort reached 2.5 cm in its largest diameter. Cells were processed and analyzed as stated above.

Sample definition and in-laboratory replication

Each graphed dot/*n* represents a biological replicate. Each *n* is stated after the corresponding figure legend section. In-laboratory replication is described for each experiment in table S4.

Statistics and data availability

No statistical methods were used to predetermine the sample size. The experiments were not randomized. The investigators were not blinded to allocation during experiments and outcome assessment. All statistical analyses were computed with GraphPad, and tests used for each experiment are listed in the figure legends. Analyses of variance (ANOVAs) with multiple comparisons between rows were corrected with Tukey's test to determine statistical significance. Two-tailed unpaired *t* tests were performed with Welch's correction.

Supplementary Materials

This PDF file includes:

Figs. S1 to S12
Tables S1 to S4

View/request a protocol for this paper from *Bio-protocol*.

REFERENCES AND NOTES

1. T. J. Curiel, G. Coukos, L. Zou, X. Alvarez, P. Cheng, P. Mottram, M. Evdemon-Hogan, J. R. Conejo-Garcia, L. Zhang, M. Burow, Y. Zhu, S. Wei, I. Kryczek, B. Daniel, A. Gordon, L. Myers, A. Lackner, M. L. Disis, K. L. Knutson, L. Chen, W. Zou, Specific recruitment of regulatory T cells in ovarian carcinoma fosters immune privilege and predicts reduced survival. *Nat. Med.* **10**, 942–949 (2004).
2. G. P. Dunn, A. T. Bruce, H. Ikeda, L. J. Old, R. D. Schreiber, Cancer immunoediting: From immunosurveillance to tumor escape. *Nat. Immunol.* **3**, 991–998 (2002).
3. D. Hanahan, R. Weinberg, Hallmarks of cancer: The next generation. *Cell* **144**, 646–674 (2011).
4. A. Angelin, L. Gil-de-Gómez, S. Dahiya, J. Jiao, L. Guo, M. H. Levine, Z. Wang, W. J. Quinn, P. K. Kopinski, L. Wang, T. Akimova, Y. Liu, T. R. Bhatti, R. Han, B. L. Laskin, J. A. Baur, I. A. Blair, D. C. Wallace, W. W. Hancock, U. H. Beier, Foxp3 reprograms T cell metabolism to function in low-glucose, high-lactate environments. *Cell Metab.* **25**, 1282–1293.e7 (2017).
5. C. M. Paluskievicz, X. Cao, R. Abdi, P. Zheng, Y. Liu, J. S. Bromberg, T regulatory cells and priming the suppressive tumor microenvironment. *Front. Immunol.* **10**, 2453 (2019).
6. N. E. Scharping, A. V. Menk, R. S. Moreci, R. D. Whetstone, R. E. Dadey, S. C. Watkins, R. L. Ferris, G. M. Delgoffe, The tumor microenvironment represses T cell mitochondrial biogenesis to drive intratumoral T cell metabolic insufficiency and dysfunction. *Immunity* **45**, 374–388 (2016).
7. M. De Simone, A. Arrigoni, G. Rossetti, P. Gruarin, V. Ranzani, C. Politano, R. J. P. Bonnal, E. Provasi, M. L. Sarnicola, I. Panzeri, M. Moro, M. Crosti, S. Mazzara, V. Vaira, S. Bosari, A. Palleschi, L. Santambrogio, G. Bovo, N. Zucchini, M. Totis, L. Gianotti, G. Cesana, R. A. Perego, N. Maroni, A. P. Ceretti, E. Opocher, R. De Francesco, J. Geginat, H. G. Stunnenberg, S. Abrignani, M. Pagani, Transcriptional landscape of human tissue lymphocytes unveils uniqueness of tumor-infiltrating T regulatory cells. *Immunity* **45**, 1135–1147 (2016).
8. G. Plitas, C. Konopacki, K. Wu, P. D. Bos, M. Morrow, E. V. Putintseva, D. M. Chudakov, A. Y. Rudensky, Regulatory T cells exhibit distinct features in human breast cancer. *Immunity* **45**, 1122–1134 (2016).
9. J. D. Fontenot, M. A. Gavin, A. Y. Rudensky, Foxp3 programs the development and function of $CD4^+CD25^+$ regulatory T cells. *Nat. Immunol.* **4**, 330–336 (2003).
10. P. Attia, A. V. Maker, L. R. Haworth, L. Rogers-Freezer, S. A. Rosenberg, Inability of a fusion protein of IL-2 and diphtheria toxin (denileukin diftitox, DAB389IL-2, Ontak) to eliminate regulatory T lymphocytes in patients with melanoma. *J. Immunother.* **28**, 582–592 (2005).
11. A. Tanaka, S. Sakaguchi, Targeting T_{reg} cells in cancer immunotherapy. *Eur. J. Immunol.* **49**, 1140–1146 (2019).
12. J. Barbi, D. M. Pardoll, F. Pan, Ubiquitin-dependent regulation of Foxp3 and T_{reg} function. *Immunol. Rev.* **266**, 27–45 (2015).
13. E. Montauti, D. Fang, Regulation of T_{reg} functions by the ubiquitin pathway. *Adv. Exp. Med. Biol.* **1278**, 47–62 (2021).
14. J. T. Cortez, E. Montauti, E. Shifrut, J. Gatchalian, Y. Zhang, O. Shaked, Y. Xu, T. L. Roth, D. R. Simeonov, Y. Zhang, S. Chen, Z. Li, J. M. Woo, J. Ho, I. A. Vogel, G. Y. Prator, B. Zhang, Y. Lee, Z. Sun, I. Ifergan, F. V. Gool, D. C. Hargreaves, J. A. Bluestone, A. Marson, D. Fang, CRISPR screen in regulatory T cells reveals modulators of Foxp3. *Nature* **582**, 416–420 (2020).

15. L. Wang, S. Kumar, S. Dahiya, F. Wang, J. Wu, K. Newick, R. Han, A. Samanta, U. H. Beier, T. Akimova, T. R. Bhatti, B. Nicholson, M. P. Kodrasov, S. Agarwal, D. E. Sterner, W. Gu, J. Weinstock, T. R. Butt, S. M. Albelda, W. W. Hancock, Ubiquitin-specific protease-7 inhibition impairs Tip60-dependent Foxp3$^+$ T-regulatory cell function and promotes antitumor immunity. *EBioMedicine* **13**, 99–112 (2016).
16. Y. Li, Y. Lu, S. Wang, Z. Han, F. Zhu, Y. Ni, R. Liang, Y. Zhang, Q. Leng, G. Wei, G. Shi, R. Zhu, D. Li, H. Wang, S. G. Zheng, H. Xu, A. Tsun, B. Li, USP21 prevents the generation of T-helper-1-like T_{reg} cells. *Nat. Commun.* **7**, 13559 (2016).
17. Z. Yang, Y. Qi, N. Lai, J. Zhang, Z. Chen, M. Liu, W. Zhang, R. Luo, S. Kang, Notch1 signaling in melanoma cells promoted tumor-induced immunosuppression via upregulation of TGF-β1. *J. Exp. Clin. Cancer Res.* **37**, 1 (2018).
18. K. de Visser, W. Kast, Effects of TGF-β on the immune system: Implications for cancer immunotherapy. *Leukemia* **13**, 1188–1199 (1999).
19. S. Fu, N. Zhang, A. C. Yopp, D. Chen, M. Mao, D. Chen, H. Zhang, Y. Ding, J. S. Bromberg, TGF-β induces Foxp3$^+$ T-regulatory cells from CD4$^+$CD25$^-$ precursors. *Am. J. Transplant.* **4**, 1614–1627 (2004).
20. T. Takimoto, Y. Wakabayashi, T. Sekiya, N. Inoue, R. Morita, K. Ichiyama, R. Takahashi, M. Asakawa, G. Muto, T. Mori, E. Hasegawa, S. Shizuya, T. Hara, M. Nomura, A. Yoshimura, *Smad2* and *Smad3* are redundantly essential for the TGF-β–mediated regulation of regulatory T plasticity and T_H1 development. *J. Immunol.* **185**, 842–855 (2010).
21. L. Lu, J. Ma, X. Wang, J. Wang, F. Zhang, J. Yu, G. He, B. Xu, D. D. Brand, D. A. Horwitz, W. Shi, S. G. Zheng, Synergistic effect of TGF-β superfamily members on the induction of Foxp3$^+$ T_{reg}. *Eur. J. Immunol.* **40**, 142–152 (2010).
22. S. Dennler, S. Huet, J.-M. Gauthier, A short amino-acid sequence in MH1 domain is responsible for functional differences between *Smad2* and *Smad3*. *Oncogene* **18**, 1643–1648 (1999).
23. A. M. Westendorf, K. Skibbe, A. Adamczyk, J. Buer, R. Geffers, W. Hansen, E. Pastille, V. Jendrossek, Hypoxia enhances immunosuppression by inhibiting CD4$^+$ effector T cell function and promoting T_{reg} activity. *Cell. Physiol. Biochem.* **41**, 1271–1284 (2017).
24. V. Kumar, D. I. Gabrilovich, Hypoxia-inducible factors in regulation of immune responses in tumour microenvironment. *Immunology* **143**, 512–519 (2014).
25. S. Chouaib, M. Z. Noman, K. Kosmatopoulos, M. A. Curran, Hypoxic stress: Obstacles and opportunities for innovative immunotherapy of cancer. *Oncogene* **36**, 439–445 (2017).
26. G. L. Semenza, Targeting HIF-1 for cancer therapy. *Nat. Rev. Cancer* **3**, 721–732 (2003).
27. E. T. Clambey, E. N. McNamee, J. A. Westrich, L. E. Glover, E. L. Campbell, P. Jedlicka, E. F. de Zoeten, J. C. Cambier, K. R. Stenmark, S. P. Colgan, H. K. Eltzschig, Hypoxia-inducible factor-1α–dependent induction of FoxP3 drives regulatory T-cell abundance and function during inflammatory hypoxia of the mucosa. *Proc. Natl. Acad. Sci. U.S.A.* **109**, E2784–E2793 (2012).
28. B. Keith, R. S. Johnson, M. C. Simon, HIF1α and HIF2α: Sibling rivalry in hypoxic tumour growth and progression. *Nat. Rev. Cancer* **12**, 9–22 (2012).
29. T. H. Kim, Y. M. Yang, C. Y. Han, J. H. Koo, H. Oh, S. S. Kim, B. H. You, Y. H. Choi, T.-S. Park, C. H. Lee, H. Kurose, M. Noureddin, E. Seki, Y.-J. Y. Wan, C. S. Choi, S. G. Kim, Gα12 ablation exacerbates liver steatosis and obesity by suppressing USP22/SIRT1-regulated mitochondrial respiration. *J. Clin. Invest.* **128**, 5587–5602 (2018).
30. K. E. Beckermann, S. O. Dudzinski, J. C. Rathmell, Dysfunctional T cell metabolism in the tumor microenvironment. *Cytokine Growth Factor Rev.* **35**, 7–14 (2017).
31. C.-H. Chang, J. Qiu, D. O'Sullivan, M. D. Buck, T. Noguchi, J. D. Curtis, Q. Chen, M. Gindin, M. M. Gubin, G. J. W. van der Windt, E. Tonc, R. D. Schreiber, E. J. Pearce, E. L. Pearce, Metabolic competition in the tumor microenvironment is a driver of cancer progression. *Cell* **162**, 1229–1241 (2015).
32. R. D. Michalek, V. A. Gerriets, S. R. Jacobs, A. N. Macintyre, N. J. MacIver, E. F. Mason, S. A. Sullivan, A. G. Nichols, J. C. Rathmell, Cutting edge: Distinct glycolytic and lipid oxidative metabolic programs are essential for effector and regulatory CD4$^+$ T cell subsets. *J. Immunol.* **186**, 3299–3303 (2011).
33. S. E. Weinberg, B. D. Singer, E. M. Steinert, C. A. Martinez, M. M. Mehta, I. Martínez-Reyes, P. Gao, K. A. Helmin, H. Abdala-Valencia, L. A. Sena, P. T. Schumacker, L. A. Turka, N. S. Chandel, Mitochondrial complex III is essential for suppressive function of regulatory T cells. *Nature* **565**, 495–499 (2019).
34. S. P. Cobbold, E. Adams, C. A. Farquhar, K. F. Nolan, D. Howie, K. O. Lui, P. J. Fairchild, A. L. Mellor, D. Ron, H. Waldmann, Infectious tolerance via the consumption of essential amino acids and mTOR signaling. *Proc. Natl. Acad. Sci. U.S.A.* **106**, 12055–12060 (2009).
35. L. A. J. O'Neill, D. G. Hardie, Metabolism of inflammation limited by AMPK and pseudo-starvation. *Nature* **493**, 346–355 (2013).
36. K. J. Condon, J. M. Orozco, C. H. Adelmann, J. B. Spinelli, P. W. van der Helm, J. M. Roberts, T. Kunchok, D. M. Sabatini, Genome-wide CRISPR screens reveal multitiered mechanisms through which mTORC1 senses mitochondrial dysfunction. *Proc. Natl. Acad. Sci. U.S.A.* **118**, e2022120118 (2021).
37. B. Shin, G. A. Benavides, J. Geng, S. B. Koralov, H. Hu, V. M. Darley-Usmar, L. E. Harrington, Mitochondrial oxidative phosphorylation regulates the fate decision between pathogenic Th17 and regulatory T cells. *Cell Rep.* **30**, 1898–1909.e4 (2020).
38. M. Tsuda, Y. Tone, C. Ogawa, Y. Nagaoka, M. Katsumata, A. Necula, D. Howie, E. Masuda, H. Waldmann, M. Tone, A bacterial artificial chromosome reporter system for expression of the human *FOXP3* gene in mouse regulatory T-cells. *Front. Immunol.* **8**, 279 (2017).
39. H. Zeng, K. Yang, C. Cloer, G. Neale, P. Vogel, H. Chi, mTORC1 couples immune signals and metabolic programming to establish T_{reg}-cell function. *Nature* **499**, 485–490 (2013).
40. A. E. Overacre-Delgoffe, M. Chikina, R. E. Dadey, H. Yano, E. A. Brunazzi, G. Shayan, W. Horne, J. M. Moskovitz, J. K. Kolls, C. Sander, Y. Shuai, D. P. Normolle, J. M. Kirkwood, R. L. Ferris, G. M. Delgoffe, T. C. Bruno, C. J. Workman, D. A. A. Vignali, Interferon-γ drives T_{reg} fragility to promote anti-tumor immunity. *Cell* **169**, 1130–1141.e11 (2017).
41. A. Köhler, E. Zimmerman, M. Schneider, E. Hurt, N. Zheng, Structural basis for assembly and activation of the heterotetrameric SAGA histone H2B deubiquitinase module. *Cell* **141**, 606–617 (2010).
42. M. T. Morgan, M. Haj-Yahya, A. E. Ringel, P. Bandi, A. Brik, C. Wolberger, Structural basis for histone H2B deubiquitination by the SAGA DUB module. *Science* **351**, 725–728 (2016).
43. J. Melo-Cardenas, Y. Zhang, D. D. Zhang, D. Fang, Ubiquitin-specific peptidase 22 functions and its involvement in disease. *Oncotarget* **7**, 44848–44856 (2016).
44. J. J. McCann, I. A. Vasilevskaya, N. P. Neupane, A. A. Shafi, C. McNair, E. Dylgjeri, A. C. Mandigo, M. J. Schiewer, R. S. Schrecengost, P. Gallagher, T. J. Stanek, S. B. McMahon, L. D. Berman-Booty, W. F. Ostrander Jr., K. E. Knudsen, USP22 functions as an oncogenic driver in prostate cancer by regulating cell proliferation and DNA repair. *Cancer Res.* **80**, 430–443 (2020).
45. C. Procaccini, F. Carbone, D. D. Silvestre, F. Brambilla, V. D. Rosa, M. Galgani, D. Faicchia, G. Marone, D. Tramontano, M. Corona, C. Alviggi, A. Porcellini, A. L. Cava, P. Mauri, G. Matarese, The proteomic landscape of human ex vivo regulatory and conventional T cells reveals specific metabolic requirements. *Immunity* **44**, 406–421 (2016).
46. J. Furusawa, K. Moro, Y. Motomura, K. Okamoto, J. Zhu, H. Takayanagi, M. Kubo, S. Koyasu, Critical role of p38 and GATA3 in natural helper cell function. *J. Immunol.* **191**, 1818–1826 (2013).
47. E. A. Wohlfert, J. R. Grainger, N. Bouladoux, J. E. Konkel, G. Oldenhove, C. H. Ribeiro, J. A. Hall, R. Yagi, S. Naik, R. Bhairavabhotla, W. E. Paul, R. Bosselut, G. Wei, K. Zhao, M. Oukka, J. Zhu, Y. Belkaid, GATA3 controls Foxp3$^+$ regulatory T cell fate during inflammation in mice. *J. Clin. Invest.* **121**, 4503–4515 (2011).
48. J. Zhang, C. Chen, X. Hou, Y. Gao, F. Lin, J. Yang, Z. Gao, L. Pan, L. Tao, C. Wen, Z. Yao, A. Tsun, G. Shi, B. Li, Identification of the E3 deubiquitinase ubiquitin-specific peptidase 21 (USP21) as a positive regulator of the transcription factor GATA3. *J. Biol. Chem.* **288**, 9373–9382 (2013).
49. A. Meng, X. Zhang, Y. Shi, Role of p38 MAPK and STAT3 in lipopolysaccharide-stimulated mouse alveolar macrophages. *Exp. Ther. Med.* **8**, 1772–1776 (2014).
50. J. Jin, J. Liu, C. Chen, Z. Liu, C. Jiang, H. Chu, W. Pan, X. Wang, L. Zhang, B. Li, C. Jiang, X. Ge, X. Xie, P. Wang, The deubiquitinase USP21 maintains the stemness of mouse embryonic stem cells via stabilization of Nanog. *Nat. Commun.* **7**, 13594 (2016).
51. S. Budhu, D. A. Schaer, Y. Li, R. Toledo-Crow, K. Panageas, X. Yang, H. Zhong, A. N. Houghton, S. C. Silverstein, T. Merghoub, J. D. Wolchok, Blockade of surface-bound TGF-β on regulatory T cells abrogates suppression of effector T cell function in the tumor microenvironment. *Sci. Signal.* **10**, eaak9702 (2017).
52. N. M. Chapman, H. Chi, mTOR signaling, T_{regs} and immune modulation. *Immunotherapy* **6**, 1295–1311 (2014).
53. G. A. Gualdoni, K. A. Mayer, L. Göschl, N. Boucheron, W. Ellmeier, G. J. Zlabinger, The AMP analog AICAR modulates the T_{reg}/T_H17 axis through enhancement of fatty acid oxidation. *FASEB J.* **30**, 3800–3809 (2016).
54. G. V. Glinsky, O. Berezovska, A. B. Glinskii, Microarray analysis identifies a death-from-cancer signature predicting therapy failure in patients with multiple types of cancer. *J. Clin. Invest.* **115**, 1503–1521 (2005).
55. Z. Lin, H. Yang, Q. Kong, J. Li, S.-M. Lee, B. Gao, H. Dong, J. Wei, J. Song, D. D. Zhang, D. Fang, USP22 antagonizes p53 transcriptional activation by deubiquitinating Sirt1 to suppress cell apoptosis and is required for mouse embryonic development. *Mol. Cell* **46**, 484–494 (2012).
56. A. Dobin, C. A. Davis, F. Schlesinger, J. Drenkow, C. Zaleski, S. Jha, P. Batut, M. Chaisson, T. R. Gingeras, STAR: Ultrafast universal RNA-seq aligner. *Bioinformatics* **29**, 15–21 (2013).
57. S. Anders, P. T. Pyl, W. Huber, HTSeq—A Python framework to work with high-throughput sequencing data. *Bioinformatics* **31**, 166–169 (2015).
58. M. D. Robinson, D. J. McCarthy, G. K. Smyth, edgeR: A Bioconductor package for differential expression analysis of digital gene expression data. *Bioinformatics* **26**, 139–140 (2010).
59. D. J. McCarthy, Y. Chen, G. K. Smyth, Differential expression analysis of multifactor RNA-Seq experiments with respect to biological variation. *Nucleic Acids Res.* **40**, 4288–4297 (2012).

Acknowledgments: We thank Fang laboratory members for critical reading of the manuscript and constructive suggestions during our research, the Northwestern Lurie Cancer Center flow cytometry core and genomic sequencing core for the service support, and the mice that gave their lives for this work. **Funding:** This work was supported by NIH R01 grants AI079056, AI108634, and CA232347 (to D.F.) and NIH National Cancer Institute (NCI) F31 CA220801 (to E.M.). **Author contributions:** E.M., S.E.W., P.C., S.C., N.L.M., R.I., Z.S., Yuan.Z., C.L., C.X., S.G., J.W., and M.Y. performed the studies and analyzed the data. E.M., S.E.W., Yusi.Z., Yana.Z., Z.S., W.C., M.Y., and D.F. designed the study and wrote the manuscript. **Competing interests:** The authors declare that they have no competing interests. **Data and materials availability:** All data needed to evaluate the conclusions in the paper are present in the paper and/or the Supplementary Materials. RNA sequencing data for *Usp21* KO and *Usp22*/*Usp21* dKO mice are deposited in GEO with accession number GSE207832. *Usp22* RNA sequencing data from Cortez *et al.* (*14*) are listed in table S5.

Submitted 8 February 2022
Accepted 26 October 2022
Published 25 November 2022
10.1126/sciadv.abo4116